MULTISCALE MODELING OF INTERWOVEN KEVLAR FIBERS BASED ON RANDOM WALK TO PREDICT YARN STRUCTURAL RESPONSE

By
STEPHEN RECCHIA

A dissertation submitted to the

Graduate School-New Brunswick

Rutgers, The State University of New Jersey

In partial fulfillment of the requirements

For the degree of

Doctor of Philosophy

Graduate Program in Material Science and Engineering

Written under the direction of

Assimina A. Pelegri

and approved by

_____

_____

_____

_____

New Brunswick, New Jersey

January, 2016

Abstract of the Dissertation

MULTISCALE MODELING OF INTERWOVEN KEVLAR FIBERS BASED ON RANDOM WALK TO PREDICT YARN STRUCTURAL RESPONSE

by STEPHEN RECCHIA

Dissertation Director:

Assimina A. Pelegri

Kevlar is the most common high-end plastic filament yarn used in body armor, tire reinforcement, and wear resistant applications. Kevlar is a trade name for an aramid fiber. These are fibers in which the chain molecules are highly oriented along the fiber axis, so the strength of the chemical bond can be exploited. The bulk material is extruded into filaments that are bound together into yarn, which may be chorded with other materials as in car tires, woven into a fabric, or layered in an epoxy to make composite panels. The high tensile strength to low weight ratio makes this material ideal for designs that decrease weight and inertia, such as automobile tires, body panels, and body armor. For designs that use Kevlar, increasing the strength, or tenacity, to weight ratio would improve performance or reduce cost of all products that are based on this material.

This thesis computationally and experimentally investigates the tenacity and stiffness of Kevlar yarns with varying twist ratios. The test boundary conditions were replicated with a geometrically accurate finite element model, resulting in a customized code that can reproduce tortuous filaments in a yarn was developed. The solid model geometry capturing filament tortuosity was implemented through a random walk method of axial geometry creation. A finite element analysis successfully recreated the yarn strength and stiffness dependency observed during the tests. The physics applied in the finite element model was reproduced in an analytical equation that was able to predict the

failure strength and strain dependency of twist ratio. The analytical solution can be employed to optimize yarn design for high strength applications.

Acknowledgements

First and foremost, I would like to express my heartfelt thanks to my advisor, Prof. Assimina A. Pelegri, for her invaluable suggestions and constantly generous support. Her encouragement and insight inspiration made this thesis possible. I would like to thank Prof. Lisa Klein, Dr. Kyran Mish, and Prof . Bernard Kear for serving as my committee members, reviewing my thesis as well as giving helpful guidance. I also thank Dr. James Zheng and Suzanne Horner for funding this research and providing the direction it needed. I gratefully acknowledge Prof. Ionnis Chassiotis for explaining fabric testing at length and sharing helpful microscopy that depicted Kevlar filament micro structure. I also thank Benjamin Spencer, Lionel Reinhardt and Dr. Jennifer Cordes for teaching me the Finite Element software used in this thesis.

I thank Max Tenorio for aiding in testing the yarn test specimens as well as acting as a sounding board for research ideas. I also thank Daniel Sullivan and Dr. Xiaodong Zhao for providing many helpful suggestions for my research.

Dedication

To my dear wife, Tamy and my loving children Eliana and Dominic.

To my beloved parents, Mr. Santo Recchia and Mrs. Peggy Recchia.

Table of Contents

List of Illustrations

List of Tables

Chapter 1 : Introduction

1.1 Kevlar as an Engineering Material

Kevlar yarn is used in a myriad of applications, from body armor to car tires. Kevlar is a trade name for an aramid fiber in which the chain molecules are highly oriented along the fiber axis, so the strength of the chemical bond can be exploited. The bulk material is extruded into filaments that are bound together into a yarn that is either chorded with other materials as in car tires, woven into a fabric, or layered in an epoxy to make composite panels. The high tensile strength to low weight ratio makes this material ideal for designs that try to decrease weight and inertia, such as automobile tires, body panels, and body armor. For designs that use Kevlar, increasing the strength to weight ratio (called Tenacity) would improve performance or reduce cost of all products that are based on this material. It has been shown [1, 2, 3, 4] that up to 3 twists per inch (TPI) the strength of Kevlar increases. As the yarn is twisted past 3TPI its strength starts to drop off making the strength to twist relationship non-linear with maximum value around 3TPI. The goal of this research is to identify the important yarn characteristics that cause the maximum strength to be at 3TPI. Kevlar fabric, chord, and yarn are all based on a fibrous structure made from filaments. There has been prior research conducted to understand the triaxiality of Kevlar KM2 filaments. [5] That research has shown that there is very little dependency of filament strength on confinement pressure due to the anisotropic nature of the elastic response. It is hypothesized that filament strain gradients between the yarn's outer diameter (OD) and core is imposed by the yarn twisting process.

1.2 Describing Kevlar Hierarchy

Through filament manufacturing aramid molecules are layered and interact with Van der Waals forces. The long molecule stacks would normally be randomly oriented when solidified but the fiber manufacturing process aligns these crystals with the fiber axis. A hypothesized Kevlar structural hierarchy is shown in Figure 1.1.

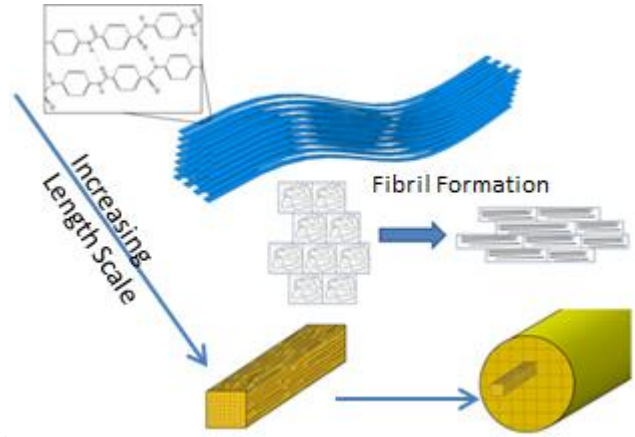

Figure 1.1 *Microfibril based structure of Kevlar showing molecular organization and hierarchy. Arrow shows increasing length scales*

Grujicic suggests that amorphous polymer and poor orientation act as grain boundaries between neatly ordered stacks [6]. These boundaries form microfibrils on the order of 10 nm in diameter. [7] Gruijicic suggests the manufacturing impurities and voids form a second layer of natural boundaries. These boundaries make fibrils that are of the order of 100-1000 nm in diameter and lengths that can reach a millimeter. The fibrils are bridged locally by microfibrils to constitute a single Kevlar fiber.

1.3 Filaments into a Yarn Structure

After filament creation, fibers are bundled into a yarn. The amount of filaments that go into a yarn structure dependents on the required linear weight and necessitated strength

from the system. Yarn strength is measured in Tenacity (gram-force/Denier) and linear weight is given as denier (g/9000m). Natural fibers like cotton, wool, or hemp are consolidated into a yarn using a ring spun method. The ring spun yarn has a twist associated with it to improve fiber to fiber interaction. Kevlar yarn is made of straight continuous filaments and the yarn is not created with a pre-twist; small twist is added to achieve a more uniform failure stress [8]. At this point the yarn can be put into larger fabric systems such as chorded rope and fabric weaves, or act as reinforcement in composites.

Chapter 2 : Method

To determine the important physics governing the yarn strength dependence on twist, a finite element model of the system was developed. Complimentary tensile testing at various twists per inch (TPI) was commenced. Based on the simulation and the tests an analytical solution is formulated to predict yarn response to twist and tensile loading.

2.1 Method: Solid Geometry Creation

A geometrically representative model was implemented to create accurate geometry and discretize it with finite elements. An explicit solver was chosen to solve the yarn stress state as the twist and axial strain boundary conditions were applied. The geometry was developed using a random walk algorithm that allowed the filaments to become interwoven. The geometry creation tool was written using Fortran 90. Commands to formulate the representative geometry in CUBIT were written into a text file that could be recounted using the GUI interface. The model was run with multiple cases that included 0, 3 and 10 twists per inch (TPI). The axial strain amplitude boundary condition was chosen so the simulation ended at filament failure. The results from the simulation were compared to tensile tests conducted using custom grips, created at the Advanced Materials Structures Laboratory (AMSL), that were mounted to an Instron universal materials testing system.

2.2 Method: Finite Element Analysis with Sierra/Solid Mechanics, (Presto)

Sierra/Solid Mechanics (Sierra/SM) is a general-purpose explicit finite element code developed and maintained by Sandia National Laboratories. It uses large deformation nonlinear Lagrangian solid mechanics principles to model the response of a wide range of structures and systems to mechanical loading. It is part of a mutli-physics suite of codes in

the Sierra framework, and can be coupled with other codes to model other types of physics. Models are defined in Sierra/SM through an ExodusII mesh and an input file that defines parameters for the analysis including materials and boundary conditions. Some of the benefits of using Sierra/SM are that it provides an extensive set of constitutive models, scalability for massively parallel computers, robust contact algorithms, and a variety of techniques for modeling pervasive failure. Details of Presto, its history, and algorithms are described in the user's manual [9] .

For the work presented here, the first step for setting up the finite element model was to create a meshing scheme of the desired geometry using the CUBIT software. Sets of elements, nodes, and surfaces were defined for assignment of material properties and application of boundary conditions, and then the mesh was exported as an ExodusII file. The Sierra/SM code used the finite element mesh and an accompanying input file defining model parameters to run the analysis, and generated results in another ExodusII file. The results of the simulation were visualized in Paraview, an open source post-processing tool developed with support from a number of organizations including Sandia National Laboratories and the U.S. Department of Defense.

In the Sierra/SM model, the yarn filaments were modeled as individual volumes built from lofted beam elements. Frictional contact was used to model the interactions between all the filaments.

2.3 Method: Finite Element Solver Theory

In Sierra Solid Mechanics [9, 10], the continuous material is numerically approximated by discretization. This is accomplished through using finite elements to build geometric representative parts. In an explicit analysis those discretized elements are connected

through nodes that have the same 6 degrees of freedom [11, 12, 13, 14]. The internal and external forces acting on those nodes are used to predict material nodal deformation. The nodal deformation is fed to the elements shape function to predict state variables such strain, stress, and damage. The nodal deformation is used to create the state variables through deviatoric, dilatational or a combination constitutive model. For an explicit analysis, this process is repeated at stable time increments that step through time during the analysis. The important physics of a dynamic explicit finite element simulation are applied through initial, steady or transient boundary conditions that modify nodal acceleration, velocity or displacement. For Sierra-SM the governing equations is stated as Equation 2.1.

$$\nabla * T + f = \rho a \tag{2.1}$$

where $\Delta * T$ denotes the divergence operator applied to the Cauchy stress tensor T. The vector f denotes the distributed body force in the body, ρ is the density and a is the acceleration. The solver simplifies the geometrically complex problem by solving simple motion equations for material particles in space. Fixing the reference coordinate $\boldsymbol{X}$. Equations 1 and 2 give solutions for the successive partial time derivatives of the motion $\phi(\boldsymbol{X},t)$ that provide velocity $\boldsymbol{V}$ and acceleration $\boldsymbol{A}$.

$$\boldsymbol{V}(\boldsymbol{X}, t) = \frac{\delta}{\delta t}(\varphi(\boldsymbol{X}, \boldsymbol{t})) \tag{2.2}$$

$$\boldsymbol{A}(\boldsymbol{X}, t) = \frac{\delta}{\delta t}\big(V(\boldsymbol{X}, \boldsymbol{t})\big) = \frac{\delta^2}{\delta t^2\big(\varphi(\boldsymbol{X}, \boldsymbol{t})\big)} \tag{2.3}$$

To calculate the state variables located on the elemental integration point the Cauchy stress tensor (Figure 2.1) is used, denoted as $\boldsymbol{T}$, it relates a unit length direction vector $\boldsymbol{n}$ to the

stress vector $\boldsymbol{T^{(n)}}$ across a surface perpendicular to $\boldsymbol{n}$. It is used for the stress discretization of elements within solids undergoing small deformations Equations 2.4 to 2.6 show the formulation for the Cauchy stress tensor.

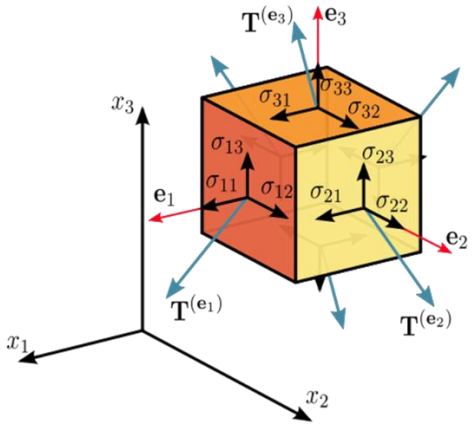

$$T^n = n * \sigma \tag{2.4}$$

$$\sigma = \begin{matrix} \sigma_{11} & \sigma_{12} & \sigma_{13} \\ \sigma_{21} & \sigma_{22} & \sigma_{23} \\ \sigma_{31} & \sigma_{32} & \sigma_{33} \end{matrix} \tag{2.5}$$

$$\begin{matrix} T_1 \\ T_2 \\ T_3 \end{matrix} = \begin{bmatrix} \sigma_{11} & \sigma_{12} & \sigma_{13} \\ \sigma_{21} & \sigma_{22} & \sigma_{23} \\ \sigma_{31} & \sigma_{32} & \sigma_{33} \end{bmatrix} \begin{bmatrix} n_1 \\ n_2 \\ n_3 \end{bmatrix} \tag{2.6}$$

Figure 2.1 *Diagram depicting the Cauchy tensor [10].*

For explicit FEA implementations large deformations are of interest so the Piola-Kirchhoff stress tensor ($\boldsymbol{P}$) is used to express stress values relative to the reference configuration instead of present configuration like Cauchy. It is calculated from the deformation gradient ($\boldsymbol{F}$), Jacobian determinate of $\boldsymbol{F}$ ($\boldsymbol{J}$),

Piola-Kirchoff Stress Tensor

$$\boldsymbol{P = J * \sigma * F^{-T}} \tag{2.7}$$

$$\boldsymbol{J = detF} \tag{2.8}$$

The goal of the time stepping procedures for finite element method is to subdivide the time interval of interest into discrete intervals. Knowing the displacement (d_n), velocity (v_n) and acceleration (a_n) at time t_{in}; the solver finds d_{n+1}, v_{n+1}, a_{n+1}. The updated displacement, velocity and acceleration are found by using the alpha method of time integrators. The alpha method is referred to as the Hiber-Hughes-Taylor method of HHT

method. The HHT method is a generalization of the Newmark family of temporal integrators.

HHT Integrator using alpha integration method

$$Ma_{n+1} + (1-\alpha)F^{int}(d_{n+1}) - \alpha F^{int}(d_n) = (1-\alpha)F^{ext}(d_{n+1}) - \alpha F^{ext}(d_n) \quad (2.9)$$

$$d_{n+1} = d_n + \Delta t v_n + \frac{\Delta t^2}{2}[(1-2\beta)a_n + 2\beta\alpha_{n+1}] \quad (2.10)$$

$$v_{n+1} = v_n + \Delta t[(1-\gamma)a_n + \gamma a_{n+1}] \quad (2.11)$$

Any numerical integration method can solve the HHT algorithms; in Sierra-SM the HHT method is incorporated into the solution by using either the central differences method or trapezoidal rule. The central differences method is used for explicit solutions. This integrator is second-order accurate in time and only conditionally stable when Δt is less than a critical value. For this method the coefficient values for Equations 2.3, 2.4, 2.5 are $\alpha = 0$, $\beta = 0$, $\gamma = ½$; once these values are substituted Equations 2.12, 2.13, and 2.14 are obtained.

HHT Integrator (Explicit Method)

$$a_{n+1} = M^{-1}F^{ext}(d_{n+1}) - F^{int}(d_{n+1}) \quad (2.12)$$

$$d_{n+1} = d_n + \Delta t v_n + \frac{\Delta t^2}{2} a_n \quad (2.13)$$

$$v_{n+1} = v_n + \frac{\Delta t}{2}[a_n + a_{n+1}] \quad (2.14)$$

The trapezoid rule integrator is used for the implicit finite element solver. This integrator is second-order accurate in time and unconditionally stable for linear problems, a problem which is defined as the spectral radii of the integrator remains less than one in modulus for any time step Δt. The coefficients for this method are $\alpha = 0$, $\beta = ¼$, $\gamma = ½$. By substituting those values into the above expressions, Equations 2.15, 2.16, and 2.17 are obtained.

HHT Integrator (Implicit Method)

$$Ma_{n+1} + F^{int}(d_{n+1}) = F^{ext}(d_{n+1}) \tag{2.15}$$

$$d_{n+1} = d_n + \Delta t v_n + \frac{\Delta t^2}{4}[a_n + a_{n+1}] \tag{2.16}$$

$$v_{n+1} = v_n + \frac{\Delta t}{2}[a_n + a_{n+1}] \tag{2.17}$$

For an Explicit analysis, the central differences method is used to calculate the displacement given acceleration and an initial state. Given the three vectors a_n, v_n, d_n, the data (a_{n+1}, v_{n+1}, d_{n+1}) at t_{n+1} can be computed explicitly as long as M is a lumped sum diagonal matrix. The HHT Explicit method was slightly modified to fit the central difference form.

HHT Integrator (Explicit Method)–Central Difference

$$a_n = M^{-1}F^{ext}(d_n) - F^{int}(d_n) \tag{2.12}$$

$$v_{n+\frac{1}{2}} = v_{n-\frac{1}{2}} + \frac{1}{2}\left[\Delta t_{n-\frac{1}{2}} + \Delta t_{n+\frac{1}{2}}\right] a_n \tag{2.13}$$

$$d_{n+1} = d_n + \Delta t_{n+\frac{1}{2}} v_{n+\frac{1}{2}} \tag{2.14}$$

The integration method is called a central difference integrator because calculates displacement in half steps as shown in the Figure 2.2. This figure shows the steps taken for each element and each time increment by the central difference operator. Step 1, the first half velocity (based on boundary conditions) is used to calculate a half increment displacement. Step 2, the half increment velocity is used to project the acceleration into the second half of the increment. Step 3, the second half velocity is calculated off the acceleration. Step 4, the displacement is calculated from the second half velocity.

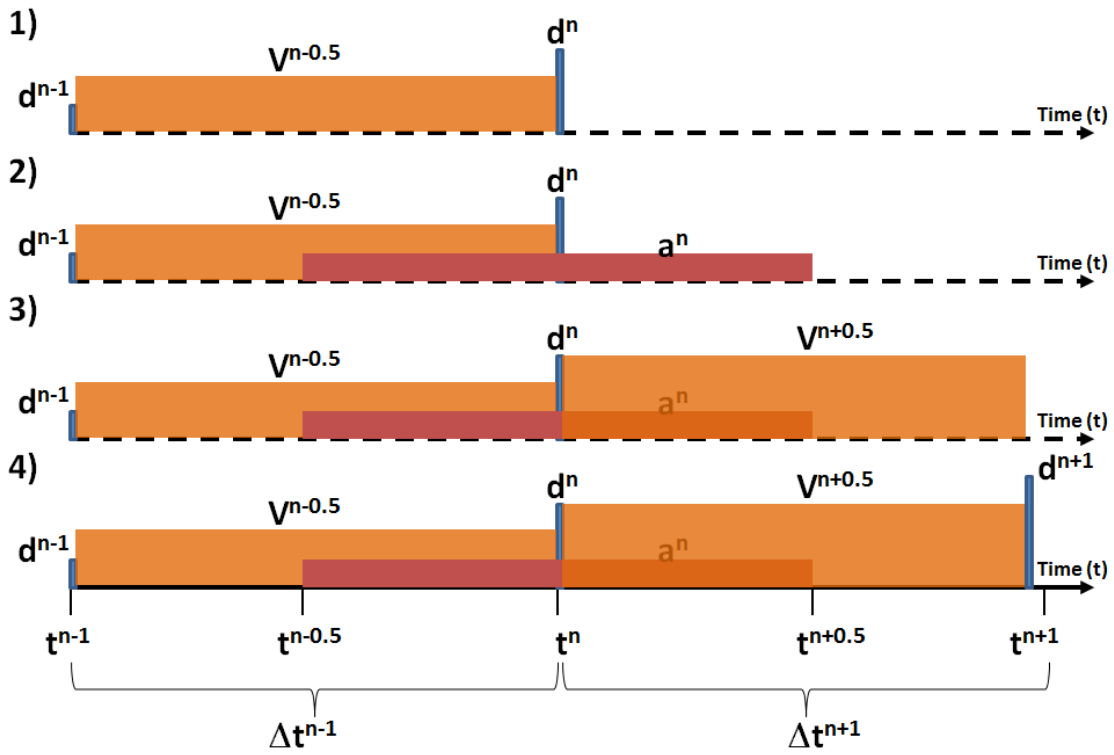

Figure 2.2 *Diagram showing the steps to calculate an element solution for a given time increment using the central differences method.*

The central differences method is conditionally stable while the time step is smaller than a critical value. The methods to evaluate a critical times step is given in Equation 2.15.

Courant Time Step	**Courant Time Step Estimation**	**Element Eigen Value Time Step Estimation**	
$\Delta t \leq \frac{2}{\omega}$	$\Delta t^{max} = \left(\frac{h}{c}\right)$	$\Delta t^{E} = \left(\frac{2}{\sqrt{\lambda}_{\max over\ e}}\right)$	(2.15)

This critical step is commonly estimated by the Courant time step criteria, where omega is the highest natural frequency in the mesh. Using the speed of sound *c* and element critical length *h*, the time step is estimated repeatedly throughout the simulation to account for geometric deformation and material change. Other ways of estimating the time step are sometimes used such as the element Eigen value time step estimation [15]. This calculation takes longer to compute but results in a larger time step since model efficiency balances time increment value with the CPU time to compute one increment. Sierra-SM allows the user to choose which time step estimation to employ in the simulation. Sometimes it is advantageous to scale the mass (density) elements to achieve slower sound speeds thus creating larger time increments. To take advantage of mass scaling the solver should employ the Eigen value time estimation .

2.4 Method: Test Kevlar KM2 at Various Twist

To probe tenacity as a function of TPI for 600 denier Kevlar KM2, grips compliant with ASTM-D-7269 were created. They were installed on a 1kN Instron 4411 universal testing apparatus. The cross head load and elongation was output from Instron software and post

processed in Excel. The yarn tests specimens were preconditioned and conditioned as per the ASTM-D-1776 standard. The preconditioning was at 3 hours 45°C with 15% relative humidity, the conditioning was at 13 hours at 20°C with 64% relative humidity.

The current grips were designed to keep the yarn aligned as it was elongated. It was assumed that the rubberized plastic coating would provide enough friction force to keep the fiber bundles sufficiently gripped. While it did perform this task well, the coating could not withstand multiple tests and ended up degrading rather quickly after a number of tests. Additionally, the edges of the grips acted as pinch points, which possibly caused early breakage. New grips have been designed that alleviated most of these issues. The new design incorporated removable faces that allowed a number of different grip surfaces to be tested, but primarily thin adhesive-backed textured rubber was used. All edges were rounded in order to prevent pinch points and an alignment groove was included to facilitate perfect alignment while provided enhanced grip action. The second generation grips designed for our experiments are depicted in Figure 2.3.

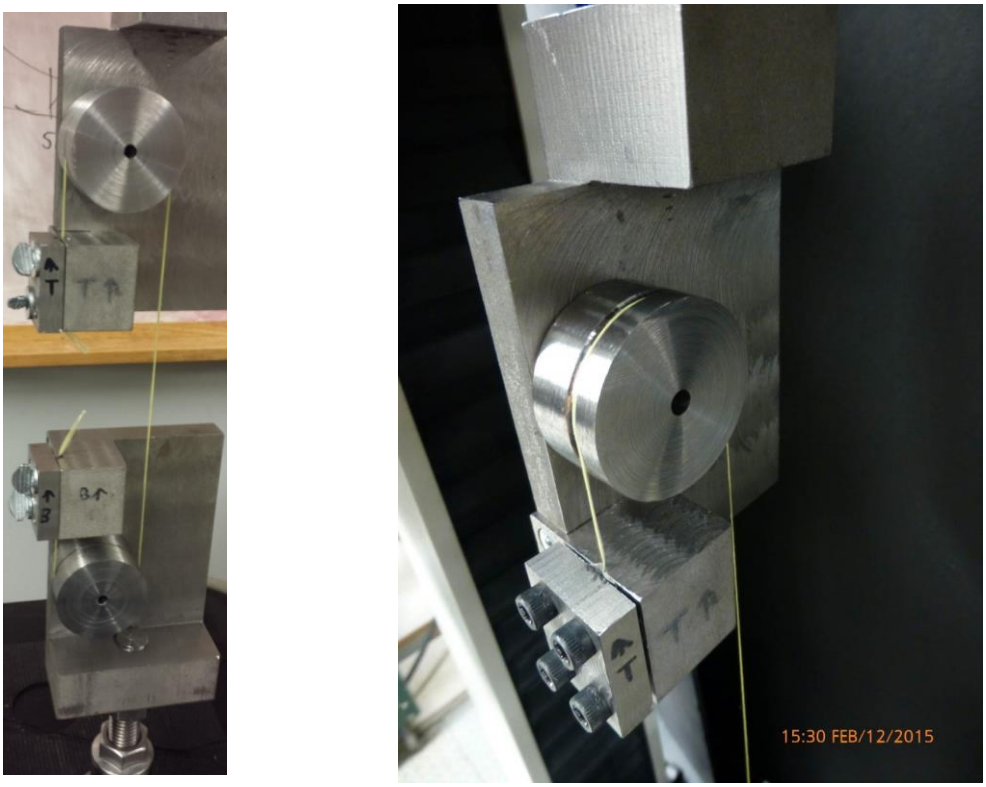

(a) **(b)**

Figure 2.3 *(a) Grips used to conduct tensile pull tests on the Kevlar KM2 fiber. (b) Close up image of grip and alignment cylinder.*

Chapter 3 : FiberWalk: a Random Walk Approach to Fiber Representative Volume Element Creation

3.1 Abstract

Attaining accurate representative geometry for a finite element analysis at various scales can be a challenging research task. Added complications arise when the geometry is representing a manufactured or biological composite. In this study, a representative geometry of linear fibrous composites was created at the microscale and is employed to reproduce crystalline micro-fibril stacking of Kevlar to form a single fibril joined by a non-ordered crystal structure. The structure can have ellipsoidal or rectangular micro-fibrils

stacked in ellipsoidal or rectangular fibrils, and may have any desired packing ratio within the 1-100% range. In order to grow a fibrous structure along a path a Random Walk methodology was used. Since the directionality of the fibers is random, but always stepping from one side of the path towards the other, the fibers can wind around each other and tangle or terminate if needed. Another key concept of this method is the addition of a rotation matrix operation for the path of the fibers. This allows the path around the three local coordinates to be in a linear or sinusoidal direction. The resultant geometry produced can represent the tortuous path nanofibrils undergo. Moreover, rotation about the path axis allows for the twisted geometry of ring spun yarn, and metal cable to be reproduced. Inclusion of spherical objects to the path of the fibers has been accommodated to reproduce fiber growth around, or end at, an obstruction in their path. This approach allows representing impurities at the fibril, fiber or yarn level of composite fabric manufacturing.

3.2 Keywords

composites, fibers, micro fibrils, multiscale simulations, nanostructure

3.3 Introduction

Representative Volume Elements (RVE) are often used by researchers for capturing micro-scale phenomena such as bulk response of randomly oriented chopped fiber composites [17], micromechanical damage of brittle solids [18], volume compaction of periodic porous composites [19], bulk material response predictions of carbon nanotube-based composites [20], and fiber reinforced fracture of polymer-matrix composites [21, 22, 23, 24] The

ability to construct an RVE becomes more complicated as the intricacy of the composite architecture increases. One such example is a Kevlar fiber (dia. ~1mm), made up from fibrils (dia. ~10um). The fibril is in turn made up of micro-fibrils (dia. ~10nm). Thus, a fibril filled with staggered micro-fibrils, as is the case of natural and man-made fibers, is a challenging RVE (see Figure 3.1). The micro-fibrils interact through Van der Waal forces and undergo damage as they are peeled apart [25].

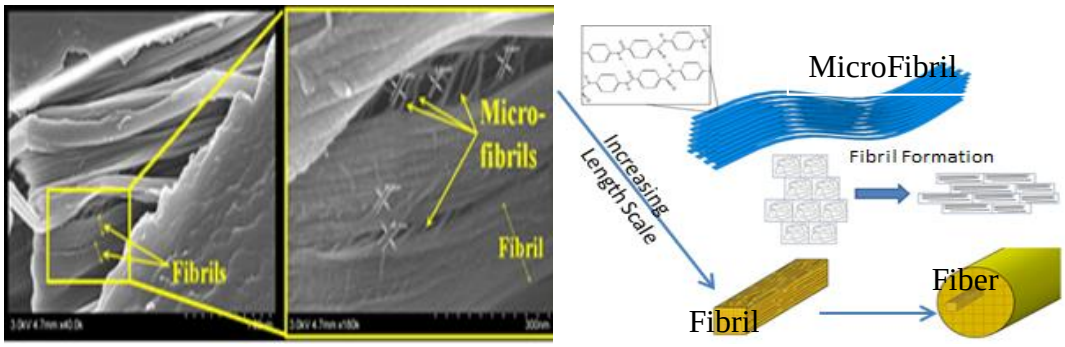

Figure 3.1 *RVE of damaged micro-fibril. Cross section of a Kevlar fiber after failure showing fibrils and microfibrils of 5-10 nm diameter* ***[23]*** *(left); and microfibril based structure of Kevlar showing molecular organization and hierarchy (right). Arrows denote increasing length scales.*

Generating an RVE composed of random chopped fibers is nearly unmanageable by manual geometry creation because of the 3-D nature of the splines, high packing density, and tortuosity and interweaving. Researchers have created complex algorithms to get high packing density of arbitrary shapes [26, 27, 28, 29]. These algorithms use a random orientation to pack the particles inside a volume, but often result in particle overlapping and can only pack aspect ratios (length/diameter) close to 1 [30].

Previously generated python scripts for high volume fraction random chopped fiber RVE creation was undertaken by Pan et al. [17] These scripts can accomplish volume fractions up to 55% for fibers of large aspect ratios close to 10. The amount of intertwining that the Pan et al. algorithm can handle although adequate for traditional composites it is not optimal, and the volume fraction obtainable is unable to handle volume fractions approaching 85 to 99%, which can be found in advanced nanocomposite structures and in biological materials. There have been many RVEs that capture fabric and yarn properties [31, 32, 33, 34]. The fabric methodologies try to approximate the preloads and plasticity of the woven yarns in weft and warp directions. However, the yarn is presumably made of parallel fiber strands where the inter-fiber dependency due to tortuosity has been overlooked due to the complexity of creating the initial geometry. This research attempts to address that complex interwoven geometry.

Fiber micro-geometries that are randomly oriented and intertwined need an RVE created where a fiber is randomly entangled with its neighbors. The complexity of creating such an RVE has kept this type of geometry from being modeled in the past. Recently an algorithm that attempts to capture the random intertwining of fibers has been created [35, 36]. These random walk algorithms pack volumes with spheres then connect the spheres with cylindrical geometry. Stochastic attempts are made to get high packing densities (> 60%). In order to obtain these densities the fibers must repel one another and thus force gradients must be applied at every spherical location. One drawback of this methodology is that it cannot handle growth of fibers along a direction.

On the biomechanics front fibrous structures are found in the brain, muscles, and other tissues. Within the last five years, researchers have improved their ability to map

axonal pathways in areas such as the spinal cord and the brain with MRI imaging. At the same time mechanical properties for local and bulk tissue response are being determined. With the improved understanding of geometry and mechanical properties, human tissue RVEs are being created to capture the tissue's non-linear response [37, 38, 39, 40, 41]. These RVEs are used to predict changes in bulk white matter response due to local axonal damage. The tortuosity of the axons is captured in the simulations by adding parallel waviness. A shortcoming of these models is that they ignore the axons being interwoven and the effect of axons being grown around soft oligodendrocytes (type of brain cell).

This paper describes a new method of random walk that has been applied to creating natural yarn and fibers by growing them along a direction. The approach taken in this paper grows the fibers along one direction mirroring what happens in natural processes. Growing along a direction simplifies the algorithm proposed by Altendorf [35]. Bulk movement of the yarn is handled by trajectories being passed through a rotation matrix. In what follows, the FiberWalk methodology is introduced, which can produce complicated fiber RVE geometries in minutes that would be extremely time and labor intensive if produced manually. Analyses using the FiberWalk subroutine are able to capture the stress localization that is important to the final yield strength and modulus of yarn (see Figure 3.2).

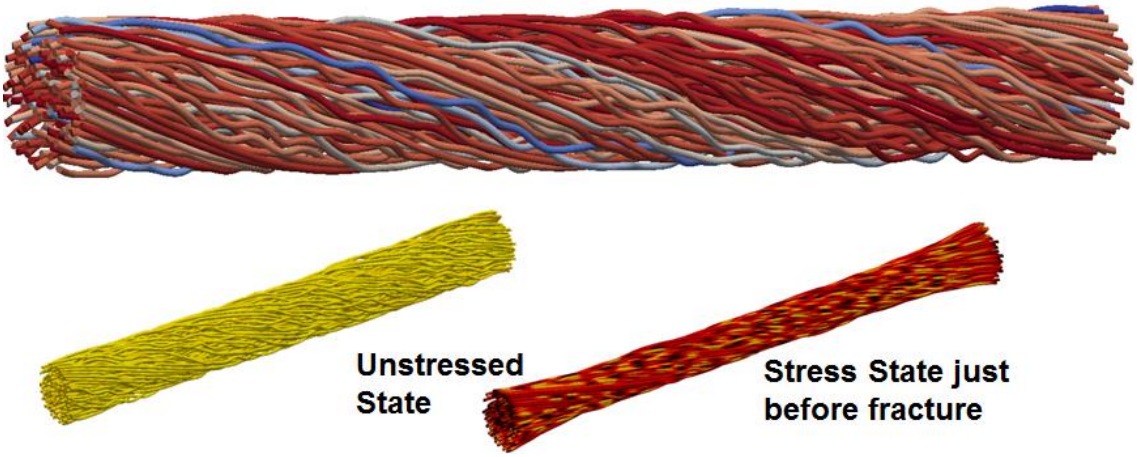

Figure 3.2 *RVE geometry (top) created by output of the RandomWalk subroutine. RVE comparison (bottom) between stressed and unstressed states. The stressed state indicates stress localizations due to intertwining of fibers.*

3.4 Mutli-Scale Geometry Generation Using Fiberwalk Method

The RandomWalk algorithm described in this paper is implemented in the FibrilPack, an RVE creation tool, developed by Pelegri's group at Rutgers Advanced Materials Structures Lab's (AMSL) .The FibrilPack program is written in Fortran 90 as a modular code that takes an input deck and feeds geometric values to an RVE algorithm (see Figure 3.3). Once the algorithm has determined x,y,z coordinates for each object, the data is then passed to a geometry and mesh creation module. The geometry creation module can either produce a Cubit and/or Abaqus python script (see Figure 3.4). When these scripts are run in their respective programs, the geometry is created and automatically meshed.

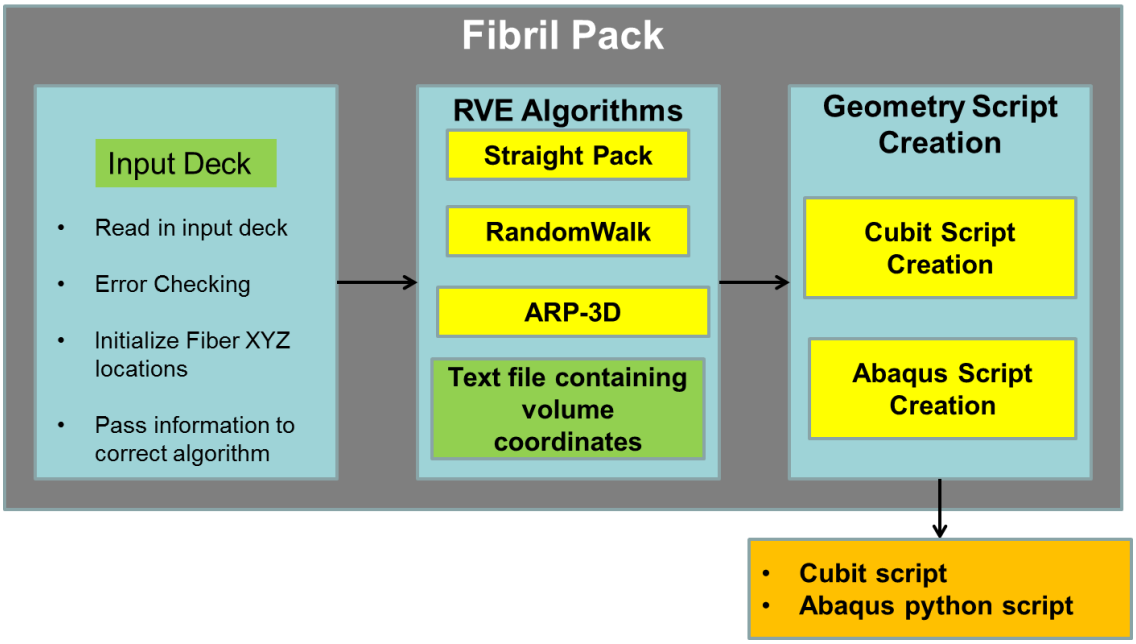

Figure 3.3 *Workflow showing how geometry input is processed through the Fibril Pack RVE creation tool. The currently available algorithms are Straight Pack, RandomWalk, Arbitrary Random Packing in 3D (ARP-3D) and inputting a text file containing XYZ points. The available geometry and mesh scripting options are Abaqus and Cubit.*

The RandomWalk algorithm, workflow depicted in figure 3.4, uses multiple planes along the axis of the cylinder or box that is being filled by the fibers. Each plane is filled with a hexagonal (bee-hive) grid and the spacing is an input into the algorithm. The direction each fiber from plane to plane is randomly chosen to create tortuosity in the fiber. The hexagonal grid ensures that as the fibers are grown from one end of the volume to the other, fiber overlap does not occur.

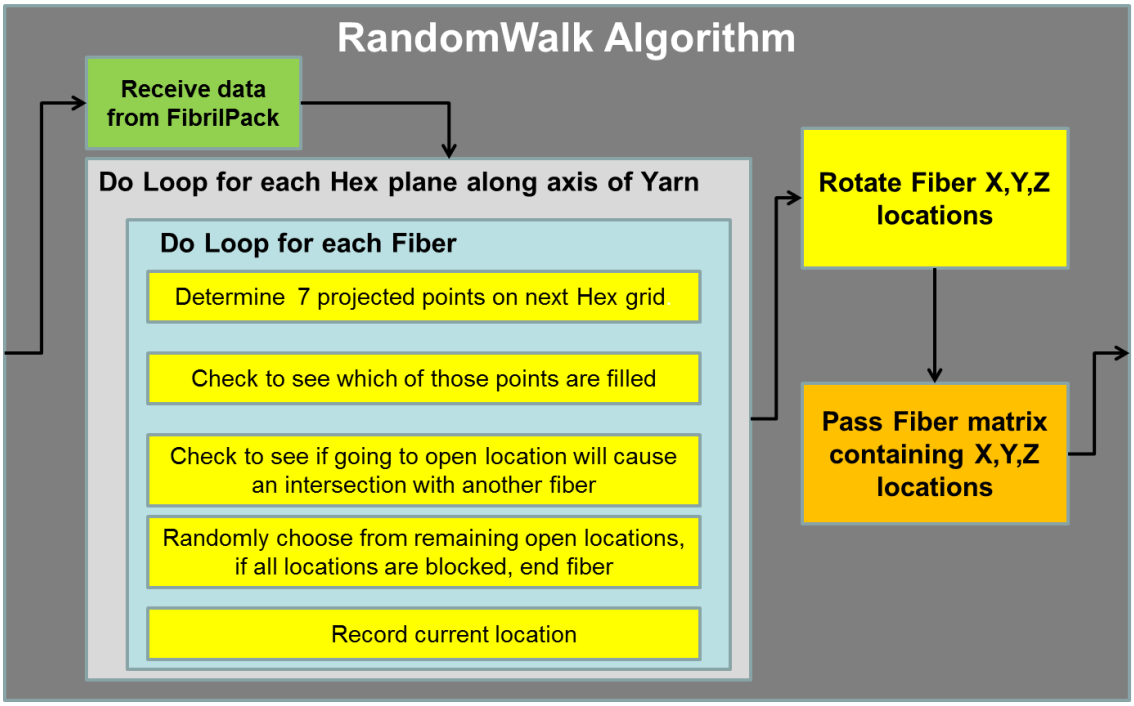

Figure 3.4 *Workflow showing how geometry input is processed through the Fibril Pack RVE creation tool. The currently available algorithms are Straight Pack, RandomWalk, Arbitrary Random Packing in 3D (ARP-3D) and inputting a text file containing XYZ points. The available geometry and mesh scripting options are Abaqus and Cubit.*

Currently allowable volume cross sections are circle or squares and allowable volume cross sections are rectangular or ellipse. The random walk method affords volume fraction from 1-100%. Intertwine of the fibers occurs at volume fractions lower than 100% due to the random nature of the fiber growth. In such a case that, a fiber gets pinched due to it being trapped between the volume boundary and neighboring fibers it is ended and restarted on the next plane. The ability to be pinched allows for much higher volume fractions to be obtained.

3.4.1 HEX Grid Technique

To create a set of fibrils that can interweave with each other (Figure 3.2) without intersecting a hexagonal grid method was chosen. The hexagon shape choice is a tradeoff between the obtainable packing density and available randomness directions (Figure 3.5). For example, a square would be more closely packed, but would only move in five possible motion vectors, and an octagon has more space around the fiber, but would have nine possible motion vectors.

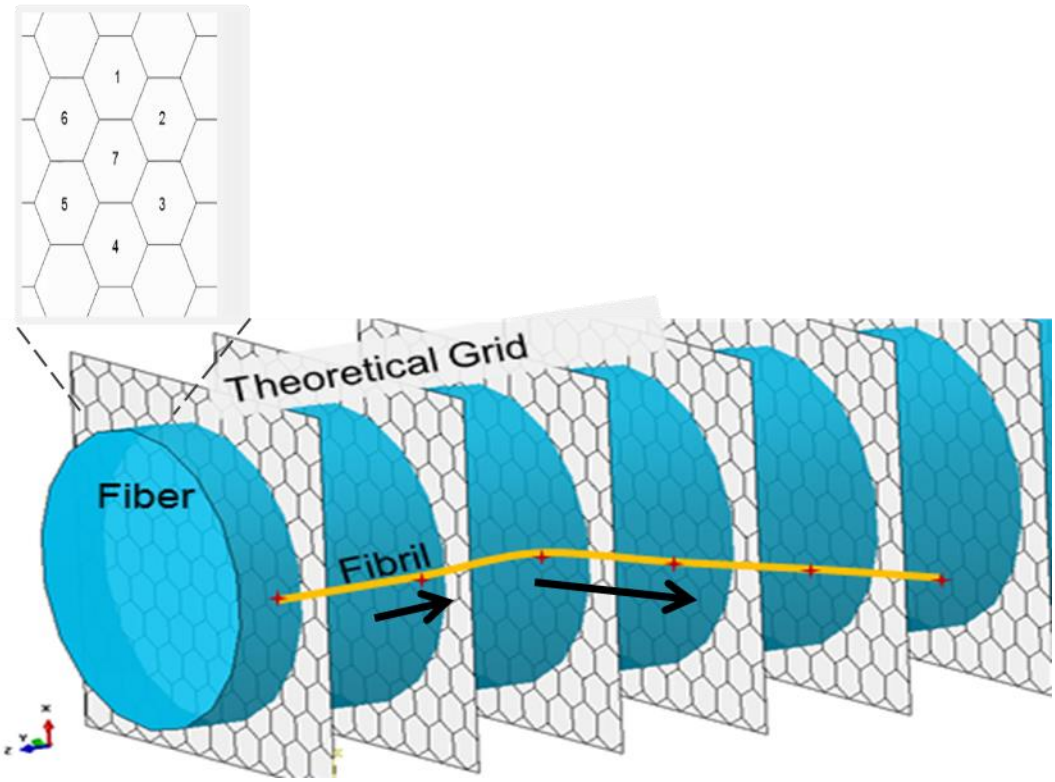

Figure 3.5 *Diagram illustrating the how hex planes are inserted across the Yarn axis. Arrows show fiber growth progression. The inset highlights the plane showing numbering for possible locations for the fibrils.*

The FiberWalk subroutine initializes the fibrils on the first plane of the fiber. Each fibril has a choice of seven possible projection hex cells on the next plane (see, inset in

Figure 3.5). The numbering starts with a purely vertical motion and proceeds clockwise until the seventh choice is straightforward. The code uses this numbering to randomly select which direction the fiber should move in.

A matrix in the FiberWalk subroutine contains all the filled hex cells. Fibrils are stopped from moving into filled hex cells. Fibers can also not move into a cell if the path crosses another fiber. These two restrictions inhibit fiber overlap. Fibrils that cannot move onto the next plane because all the spaces are filled are ended and new fibrils start at available open locations.

3.4.2 Dislocation Resolution

The term dislocation is referenced in the context of any hard or soft particle that is an inclusion to an interwoven fibrous structure. Depending on material systems used in the model, dislocations can be added to the RVE. Dislocations in the RVE can be oligodendrocytes surrounded by axons in white matter [42] [39], chaff in cotton [43], or chemical impurities in Kevlar. Dislocations that are introduced during the creation of a yarn or composite can affect the total strength of the manufactured material [43]. The method for how a dislocation is resolved in the grid can cause possible overlap issues with the final geometry. This is primarily due to splines connecting fiber locations and the size of the hex spacing. If a dislocation only partially overlaps a space in the hex grid, there is a chance that a fiber will move into that space causing interference. Therefore, a boundary layer that is sized as a function of grid spacing and dislocation size is introduced to the FiberWalk subroutine to ensure the fibrils do not come into contact with the ellipsoidal object, see Figure 3.6.

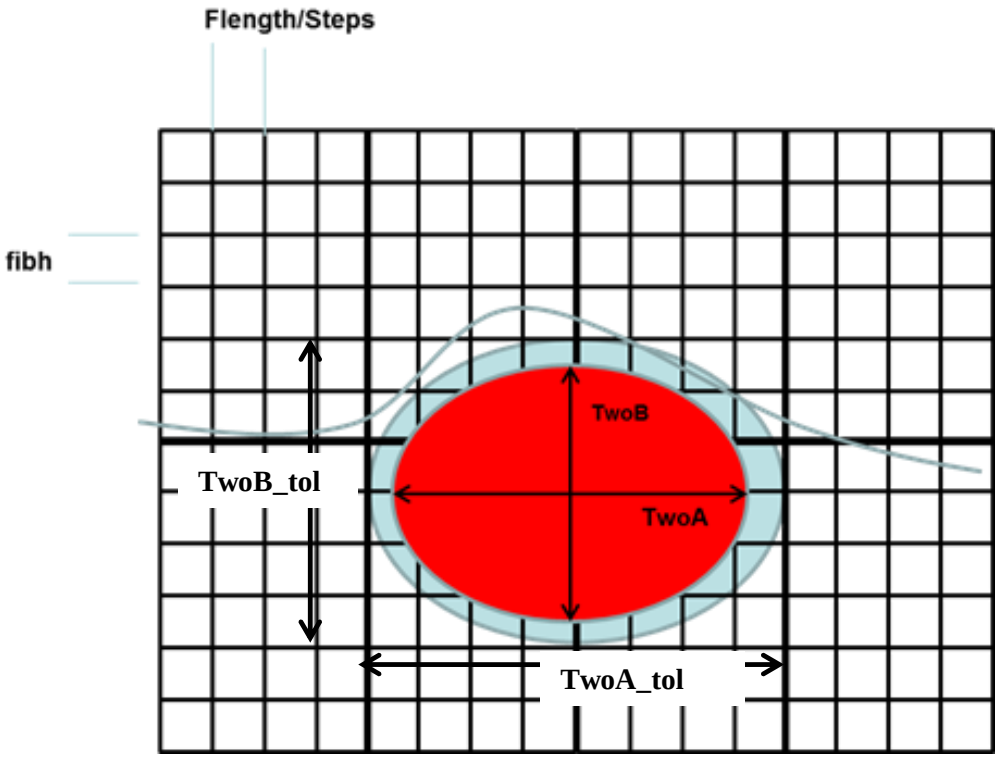

Figure 3.6 *Diagram of the dislocation (red) and tolerance boundary layer (blue). The boundary layer keeps the fiber from contacting the dislocation. The boundary layer thickness is a function of grid resolution, fiber dimensions and dislocation dimension.*

In order to guarantee that there is no overlap between the fibril and the dislocation, a boundary space the size of the grid must be created. The size of the boundary layer is intrinsically related to the resolution of the grid spacing, because as the latter increases the error due to contact avoidance decreases. The equations describing the tolerance space are

$$TwoA_{tol} = TwoA + \left(Ceiling * \frac{TwoA}{\frac{FLengt\hbar}{steps}} - Floor * \frac{TwoA}{\frac{Flengt\hbar}{steps}} \right) * \frac{Flengt\hbar}{steps}$$

$$TwoB\_tol = TwoB + \left(Ceiling * \frac{TwoB}{fib\hbar} - Floor * \frac{TwoB}{fib\hbar} \right) * fib\hbar$$

$$TwoA_{tol} = TwoA + \left(Ceiling * \frac{TwoA}{\frac{FLengt\hbar}{steps}} - Floor * \frac{TwoA}{\frac{Flengt\hbar}{steps}} \right) * \frac{Flengt\hbar}{steps} \quad (3.1)$$

$$TwoB\_tol = TwoB + \left(Ceiling * \frac{TwoB}{fib\hbar} - Floor * \frac{TwoB}{fib\hbar} \right) * fib\hbar \quad (3.2)$$

Where *TwoA_tol* and *TwoB_tol* are the major and minor access of the boundary layer surrounding the dislocation. *TwoA* and *TwoB* is the major and minor access of the elliptical prism dislocations. *Flength* is the total yarn length (Figure 3.2). *Steps* is the number of points resolving the yarn length and *fibh* is the diameter of the circular fiber (Figure 3.6). The equations show that as the grid is resolved (*fibh* and *Flength/steps* decrease), the boundary layer becomes thinner.

3.4.3 Yarn Rotation

To model a fiber with a sinusoidal shape or twisted geometry a matrix rotation option has been added to FiberWalk subroutine (see Figure 3.7).

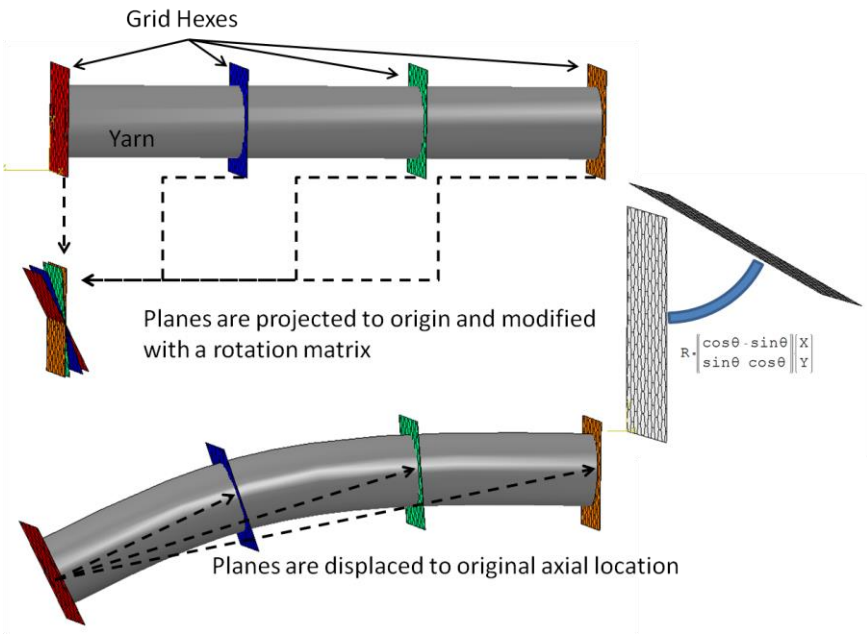

Figure 3.7 *Schematic of the hex plane rotation procedures to produce a sinusoidal or axial rotational twist of the yarn. The points on each hex plane are moved to the origin, rotated and then displaced back to their axial position.*

The final interwoven geometry can be rotated either through a sinusoidal pattern or twisted around its fiber axis (Figure 3.8). Upon completion of the FiberWalk subroutine an analysis predicting yarn strength was conducted as a proof of concept.

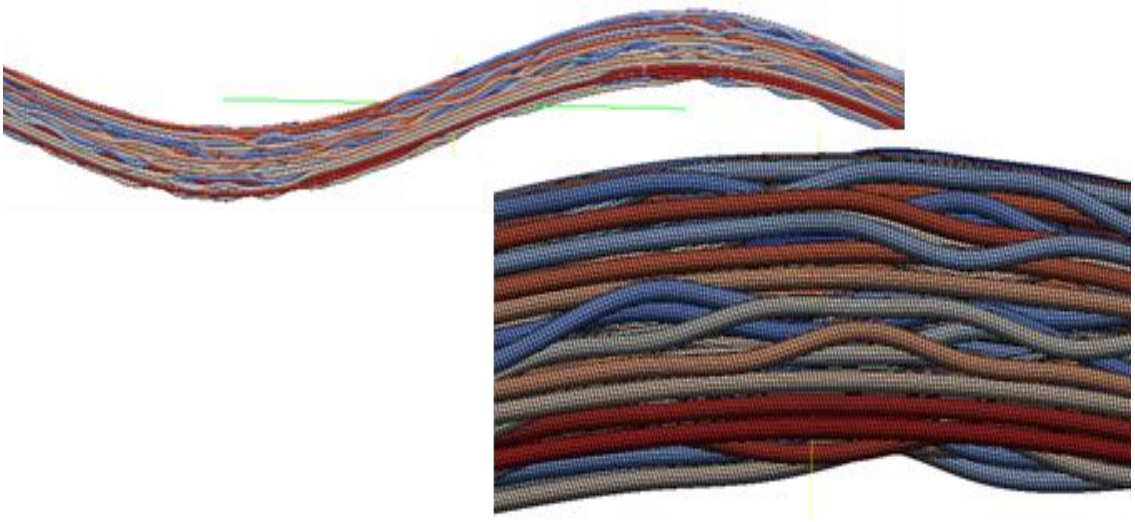

Figure 3.8 *Far (top) and Close (bottom) view of example RVE created by using the rotation matrix. This RVE is depicting a sinusoidal yarn made up of interwoven fibers.*

Man-made microstructures are often densely packed and uniform [23]. For this reason a ring spun natural fiber yarn was selected as the proof RVE. The natural fiber provides complexity that is needed to prove out the geometry creation methodology.

3.4.4 Yarn Analysis

A yarn with tortuosity and twist would add geometric complexity and be beneficial to proving the FiberWalk subroutine. The purpose of this analysis is to reproduce the fracture strength of a ring spun cotton yarn of 118 fibers while knowing only the mechanical properties of the fiber and the micro scale geometric properties of the yarn, namely, twist, fiber diameter, yarn diameter and number of fibers. The yarn gauge length for this analysis was 2 mm (Figure 3.9) because from the micrographs it was determined that this length allows the yarn to be composed of full length fibrils, that is, there are no fibrils ending within the yarn enabling us to observe stress-strain distribution along the whole path length of a fibril.

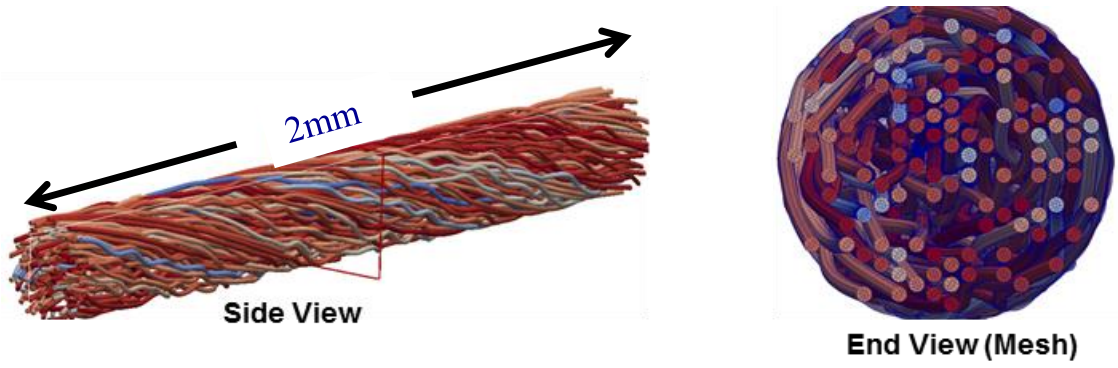

Figure 3.9 *RVE created for this analysis. (Left) 3D view of yarn length with intricate waviness and individual fibers and twist of yarn explicitly depicted; (right) 2D view of yarn cross section at designated window in the side view.*

The micrograph of ring spun cotton yarn provides the fiber diameter (13um), yarn diameter (226um), and twist angle (71^0), as seen in Figure 3.10. Note that the fiber diameter and yarn diameter follow a distribution and the average value is considered in this study as a proof of concept. In subsequent studies the distribution function will be incorporated in the analysis. To the best knowledge of the authors, there are no published SI values for single cotton fiber.

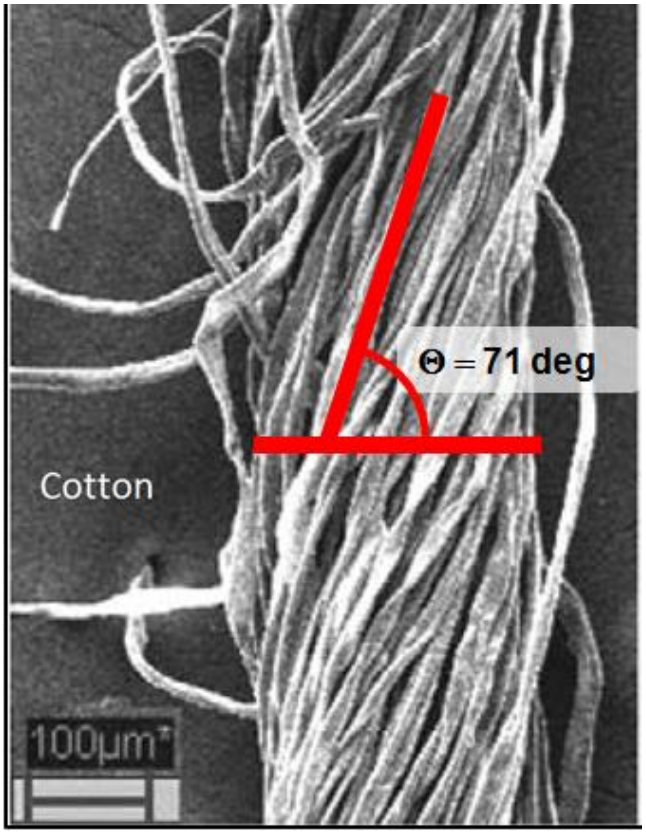

Figure 3.10 *Micrograph of 24 tex cotton yarn **[44]**, with fiber diameter of 13 um, fiber length of 28 mm, and yarn diameter of 226 □m. The angle of twist of the yarn is measured at □=71^0. The waviness of the individual fibers is also apparent and measureable.*

Therefore, the SI mechanical properties of the fiber must be translated from a textile specific unit set. Yarn manufactures use a different set of units to measure specific strength. The fracture strength is called “tenacity”, which is measured in tex (g/1000m). Tex is also used in order to describe yarn’s weight per unit length. The number of fibers in a given yarn is derived from a fiber's tex. To illustrate, if a yarn is made from cotton, is 226 um in diameter, and has a 24 tex count, then 118 fibers exist in the yarn's cross section which is considered approximately 40% packed. For cotton the dry tenacity is 1.9-3.1 cN/dtex and dry breaking extension (%) is 10 Jul for a fiber of 25-45 mm length and 1.5-1.54 g/cm^3 density [45]. These values translate to density of 1.59E-9 tonne/mm^3, fracture strength of 377.5 MPa, and elastic modulus of 4,718 MPa. The cotton material properties were used to create a linear elastic fracture constitutive model for the analysis.

3.4.5 Fiber Contact

Contact between all the fibers in the analysis is too complex to manually assign contact pairs. For this reason a general contact algorithm was employed. The Dash general contact algorithm was chosen because it is a face to face contact as opposed to a node to face method. This interaction has a friction of 0.6. A friction study was conducted to determine the best value. The friction coefficient was set to 0.1, 0.6, and 0.9. The change in the strength response was less than 5% (see Figure 3.11).

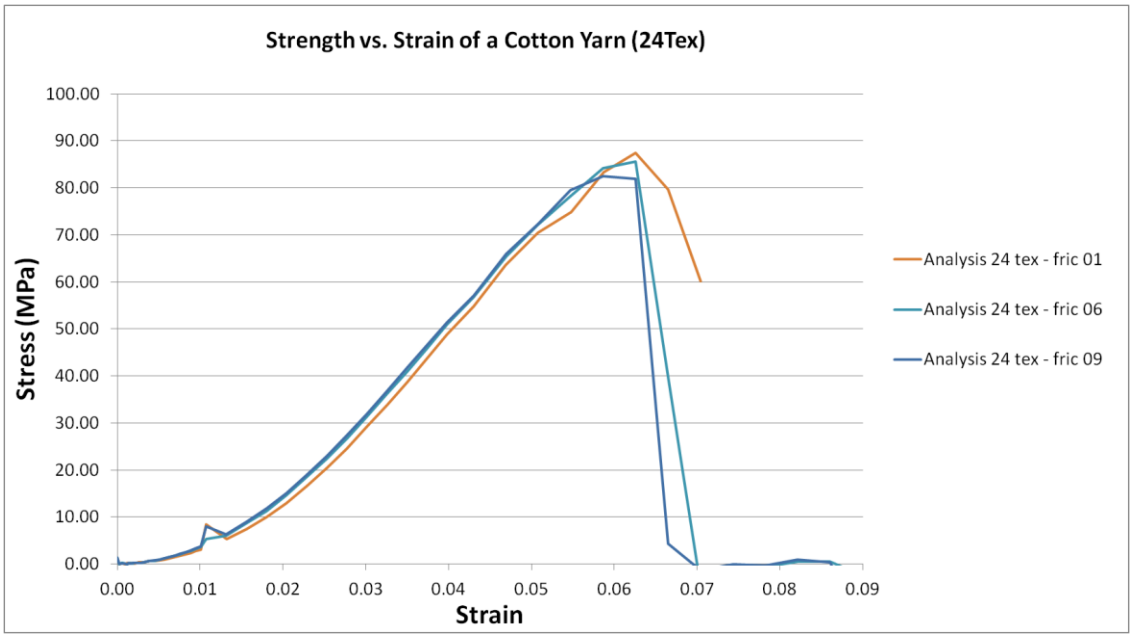

Figure 3.11 *Stress strain response of cotton yarn (24 tex) at 0.1, 0.6, and 0.9 friction coefficients. The failure strength changes by 5%. The failure slope tends to decreases as the friction increases.*

Friction is captured by the FEA model taking surface elements in contact and calculating the normal vector and force from the nodal forces of the surface element. Seemingly the tortuosity of the fibrous structure is more significant to the resultant yarn force than fiber on fiber friction. Since the fibers are intertwined the energy absorbed by fibers sliding is small, so there is a small dependency on the friction coefficient. The tortuosity also reduces the effective gauge length of the fiber being pulled shown by stress localizations that are higher than the total yarn stress. Each fiber with a localization absorbs a higher amount of energy than a fiber would with less entanglement. In the general contact algorithm all the fiber volumes are skinned (a surface set is created that includes all the outside surfaces of each fiber) for the face to face enforcement methodology. As the yarn is stretched during the analysis, the fibers are forced together due to the twist and random

inter-weaving. The general contact keeps the fibers from overlapping and imparts the normal stress onto the contact faces (Figure 3.12).

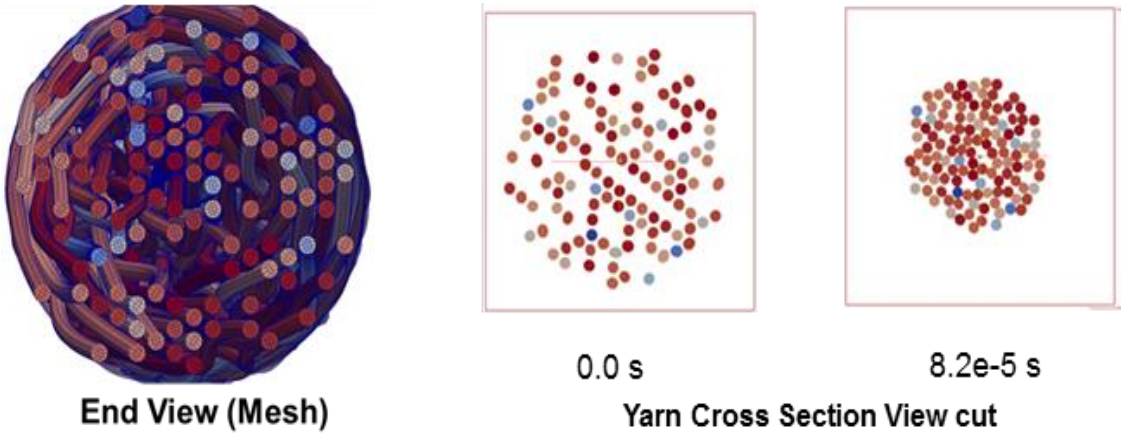

Figure 3.12 *One end view of yarn (left) and two view cuts (right) showing how contact keeps the fibers from overlapping as they are pulled together due to tensile loading.*

3.4.6 Boundary Conditions

To predict the total yarn strength the RVE was analyzed in tension. The two ends of the yarn were held fixed in the transverse direction. When the transverse directions were not fixed the yarn unwound during the tensile pull. This assumption is consistent with the clamps on a tensile machine trapping the ends and only allowing deflection in the axial direction. In the analysis the ends were pulled along the axial vector under a piecewise linear displacement boundary condition with a magnitude of 0.18mm, Figure 3.13.

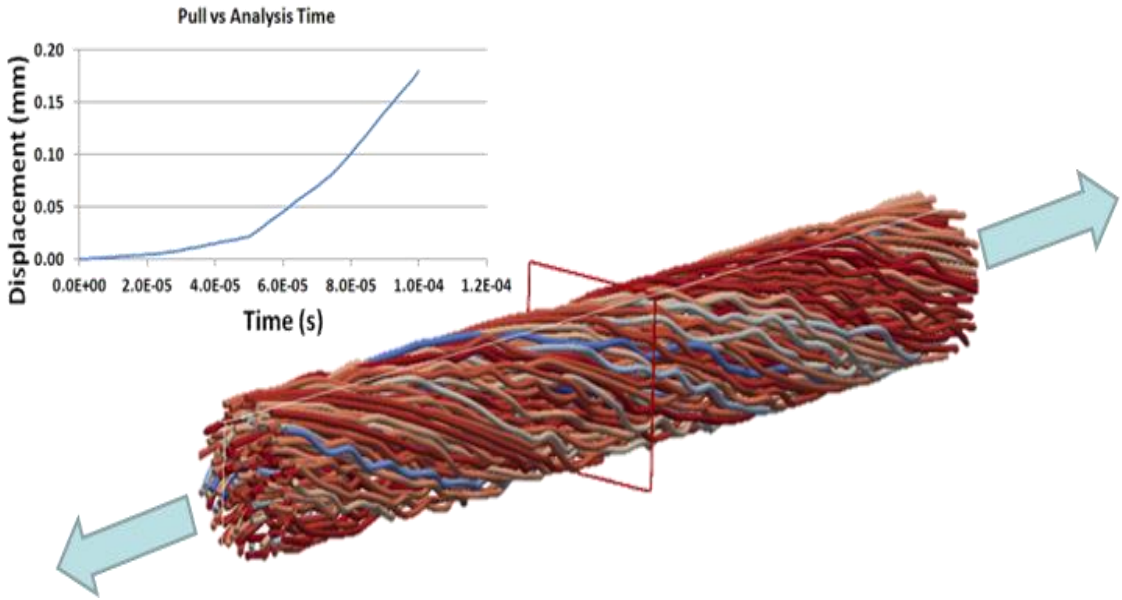

Figure 3.13 *Chart (left) showing displacement vs. time curve applied to both ends of the yarn. Arrows (right) depict direction vector of displacement.*

The non-constant displacement rate boundary condition was employed to create a quasi-static pull condition. The goal was to pull slowly to gradually overcome fiber inertia effects then pull quickly to failure in order to optimize computational time. The solver calculates the force needed to create the prescribed deflection based on material properties, geometry and architecture of the yarn and the fibers. The force applied by the solver was translated to stress and is illustrated in Figure 3.14.

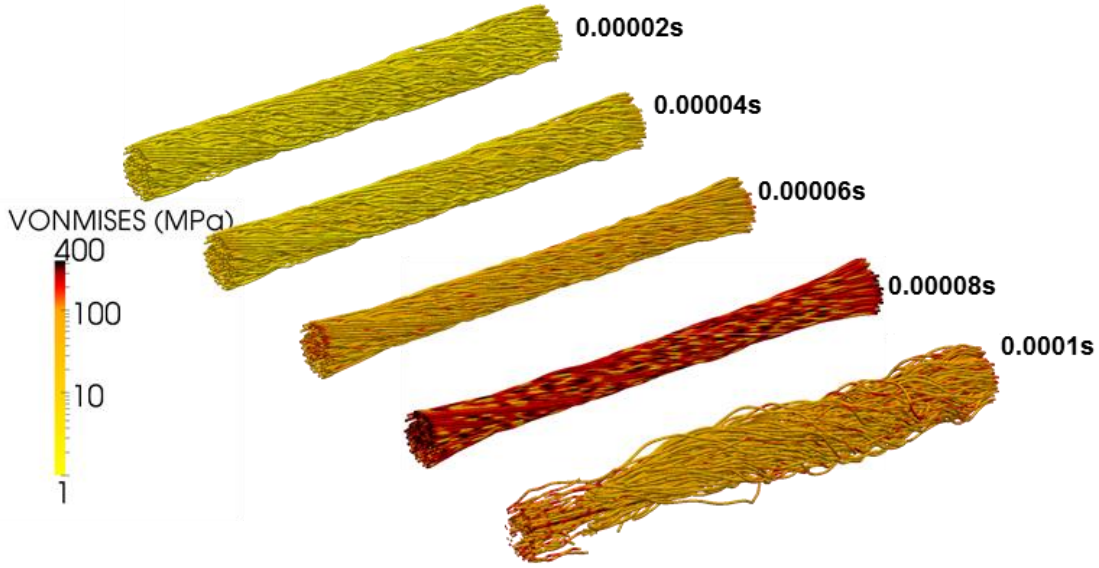

Figure 3.14 *Von Mises plots of yarn at varying times of the analysis. As the analysis progresses (top to bottom) stress points grow until fiber breakage and unwinding.*

3.5 Results and Discussion

As the analysis progressed the yarn was stretched along the longitudinal axis. Initially, the response of the yarn was non-linear with a low stiffness. When put into tension the fibers pull tight against one another due to the twist. When the fibers are transversely compressed so they are all touching (see Figure 3.12), the stiffness response of the yarn becomes linear and stiffer than the original response. The status of the Von Mises stress of a single yarn at 20, 40, 60, 80, and 100 ms is illustrated in Figure 3.14. As seen in the plots high stress localizations are ensued during stretching attributed to the tortuosity of the interwoven fibers. Initially and up to 40 ms stress localization is minimal since spacing and tortuosity between the fibers counteracts the development of high stresses. Upon the elimination of tortuosity the yarn starts to contract in the transverse direction pulling the fiber together thus increasing the local stresses. Figure 3.12 depicts the changes of the yarn cross section

between 0 ms and 82 ms; the temporal effect is illustrated in the Von Mises stress diagram of Figure 3.14. The stress localizations increase in magnitude until failure occurs. At 1% strain there is a small peak on the analysis curve shown in Figure 3.14. Subsequent analyses with a different fiber material have shown that this peak is due to the Poisson's ratio being close to incompressible or 0.45. In those analyses when the Poisons ratio was decreased the peak disappeared. A brittle fracture was set for each fiber. The strain at fracture was taken from the literature [45]. The localizations are dependent on the RVE geometry. The fibers that are interwoven pull "tight" first and have much higher stress levels. These high stresses are not seen in fibers that mostly run parallel to their neighbors. Fibers reach their respective failure points at various sequential times during the analysis. As the fibers fail one by one the stiffness of the yarn softens until they have all failed. After the fibers have all fractured the yarn unwinds, Figure 3.14.

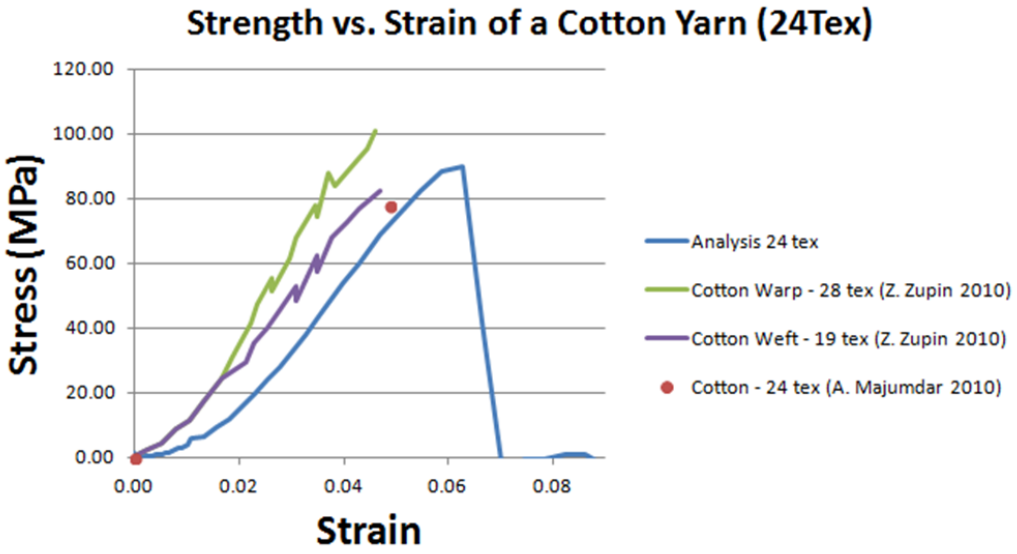

Figure 3.15 *Chart comparing Analysis of cotton 24 tex to publish results, namely, cotton – 24 tex **[44]**, and cotton warp – 28 tex and cotton weft – 19 tex **[45]**. The Failure Stress predicted by the analysis is within 15%, and the nonlinear elastic stiffness is within 5% of the published values.*

Figure 3.15 illustrates the stress versus strain behavior of a cotton yarn. In this graph the analytical results as produced from this study are presented along with results found in the literature. The comparative data are of cotton 24 tex [44] (the same as in the analysis) as well as cotton weft (one direction of the weave) 19 tex [45] and cotton warp (the other direction of a weave) 28 tex [45] are charted. Due to lack of more accurate experimental data, only trends are examined in this plot. The fact that the yarn modulus appears softer than the experimental data can be attributed to the volume fraction of the fibers in the yarn (40%.) After the fibers are pulled "tight" against each other due to the yarn twist, the model predicts a modulus that 1,851 MPa while the experimental data measured 1,846 MPa [45]. Moreover, the failure stress difference between the analysis and the experimental data by [44] is due to the tested yarn being pulled from a fabric weave. During this process the fiber is usually pre-tightened. Since it takes some distance for the yarn tightening to occur and the analysis yarn is created pristine, the analysis results are shifted to the right. The strength of the yarn on the modulus is stronger than the published tested yarn strengths. The predicted yarn fracture strength was within 15% of the experimental results. The modulus predicted by the analysis was within 0.2% of the experiment results (Figure 3.14). The yarn values from this analysis were predicted using only micro-mechanical properties and micro-structural geometry.

3.6 Conclusions

The model correlates to experimental results based on only micro scale geometry and fiber properties. The predicted linear modulus of the stress response was within 0.2% of the tested fiber. The predicted yarn strength is high by about 15%; this over prediction is most

likely due to test standard deviation in the test data and the fiber strength properties being taken from a separate research group as the yarn strength. Knowing only a small amount of micro-scale information of fiber material properties, yarn twist, and yarn tex value it is possible to use the Rutgers Fibril-Packer RVE algorithm with the RandomWalk module to create the necessary geometry to correctly model ring spun yarn strengths. Once this model is validated for pure yarns (100% cotton or 100% bamboo), it can be used to model the micro-scale response of yarn mixtures, such as 50% cotton and 50% bamboo, or any combination in between, composite fiber mixtures for advanced ballistic and armament structures, and biological systems

3.7 Acknowledgements

The authors kindly acknowledge the financial support PEO-Soldier of the United States Army Contract W91CRB-12-P-0047 P00003 to perform this research.

Chapter 4 : Multiscale Modeling of Randomly Interwove Fibers for Prediction of KM2 Kevlar Yarn Strength and Damage

4.1 Abstract

Modeling Kevlar yarn response as a function of twist requires creating a model at the filament level that incorporates capturing the mechanical interaction of numerous fibers. The inherent complexity of building multi-scale interwoven fibrous structure manually is prohibitive for such endeavor therefore computer-aided simulations are preferred. In this study, a Random Walk methodology was employed to generate a fibrous structure along the axis of a yarn. Since the directionality of the fibers is randomly oriented along the axis, the fibers can wind around each other and tangle or terminate upon demand. The resultant geometry can represent the tortuous path that yarn filaments experience. Yarn twist can be introduced through imposing a rotation matrix to the geometry or conducting an initial analysis that applies the pre-load. The analysis method employed in this paper captures the correct pre-stress of the twisted yarns at zero, three, and ten twists per inch. The analysis then loaded the yarn until filament fracture occurred. The predicted ultimate load was within 5% for all three twists per inch analyzed. The zero twists per inch linear response matched test results to within 5%.

4.2 Keywords

composites; fibers; micro fibrils; KM2 Kevlar; multiscale simulations: nanostructure

4.3 Introduction

Being able to predict the dependency of yarn tenacity on twist is critical for engineers who optimize tire chord or wear resistant fabric designs. Prediction of strength and design performance requires simulation tools capable of capturing the multi-scale physical response of the yarn to induced twist [47]. It has been observed that the yarn strength increases to around 3 twists per inch (TPI) then decreases as the TPI continues to increase [48, 8]. The research described in this paper attempts to explain the yarn strength as a function of twist. In order to capture enough physics to have a prognostic model, a Representative Volume Element (RVE) model was created from the filament level with the yarn being modeled as a fibrous structure of filaments.

Representative volume elements are most commonly used to model the bulk response of randomly oriented chopped fiber composites [17], bulk material response predictions of carbon nanotube-based composites [20], and fiber reinforced fracture of polymer-matrix composites [21, 22, 49, 24]. The ability to construct an RVE becomes more complicated as the intricacy of the composite architecture increases. For instance, Kevlar yarn (dia. ~0.7mm) is manufactured by an assembly of fibers (dia ~0.01mm) and each fiber is composed of fibrils (dia. ~10um), which in turn are constructed of micro-fibrils (dia. ~10nm) [50, 51, 52].

Several RVEs that capture fabric and yarn properties such as tenacity and load at failure have been devised [31, 32, 33, 34, 53, 54, 6]. Fabric methodologies often focus on the fabric creation and assume that the yarn is made from parallel strands. They focus

mainly on approximating the preloads and plasticity of the woven yarns in the two perpendicular in-plane weave directions defined as weft and warp. The yarn in the above papers is made of parallel fiber strands where the inter-fiber dependency caused by tortuosity has been overlooked. It is theorized that this is due to the complexity of creating the initial geometry. The research described in this paper advances from the fabric weave level to that of a yarn to address the complex interwoven geometry.

Fiber micro-geometries that are randomly oriented and intertwined necessitate the structure of an RVE in which a fiber is randomly entangled with its neighbors. The complexity of creating such RVEs has kept this type of geometry from being modeled in the past. Recently an algorithm that captures the random intertwining of fibers has been developed [35, 36]. The referenced random walk algorithms pack volumes with spheres, which are consequently connected with cylindrical geometry. Stochastic trials are made to get high packing densities (> 60%) by allowing the fibers to determine a starting location and path by imposing force gradients at every spherical location.

Here, a new method of random walk is developed to create a natural yarn and its constituent fibers by projecting them along a direction. The approach projects the fibers along one direction mirroring what happens in natural processes such as tissue generation. Projecting fibrous microstructures along a direction simplifies the algorithm proposed by Altendorf [35]. By giving up randomness in one direction the model is able to create cylindrical fibrous structures. These structures are applicable for building yarns, cables, and bundled geometries. Bulk movement of the yarn is handled by trajectories being passed through a rotation matrix. In what follows, the FiberWalk methodology is introduced,

which can produce complicated fiber RVE geometries in minutes that would be prohibitively time and labor intensive if produced manually.

4.4 Randomly interwoven Fibrous Yarn geometry creation

The RandomWalk algorithm used in this paper is implemented in the FibrilPack, an RVE creation tool. This tool seeds building block start points at varying percentages in an ellipsoidal or rectangular shape. Those seed points are projected along an axis either by a 3D structured methodology (brick wall) or a random walk method (interwoven vines). The elliptic cylinder or rectangular geometry is then passed through a rotation matrix to allow twist along axis or sinusoidal behavior. Tire chord creation can be easily added to the rotation matrix step given an axis of rotation measured from the yarn axis.

The FibrilPack program is written in Fortran 90 as a modular code that takes an input deck and feeds geometric values to an RVE algorithm (see Figure 4.1).

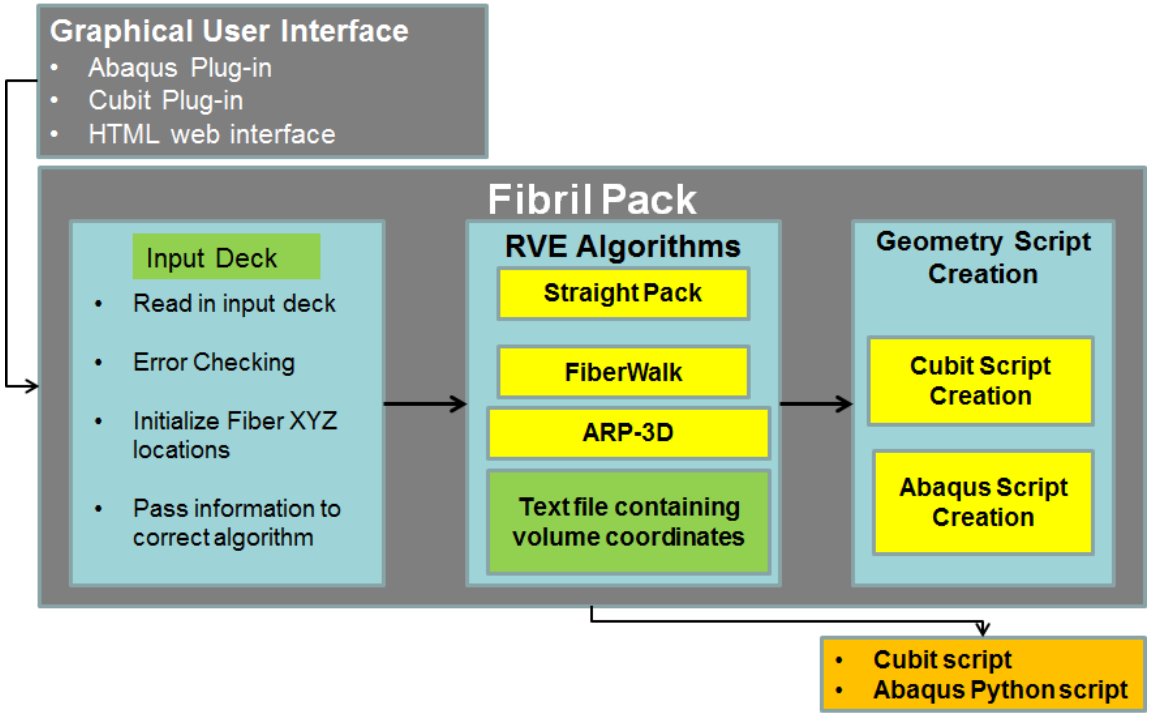

Figure 4.1 *Workflow depicting geometry input processing through the Fibril Pack RVE creation tool. The currently available algorithms are Straight Pack, RandomWalk, Arbitrary Random Packing in 3D (ARP-3D), and they input a text file containing xyz points. The available geometry and mesh scripting options are Abaqus and Cubit.*

Once the algorithm has determined x,y,z coordinates for each object, the data is then passed to a geometry and mesh creation module. The geometry creation module can either produce a Cubit or an Abaqus Python script (see Figure 4.2) [55] .

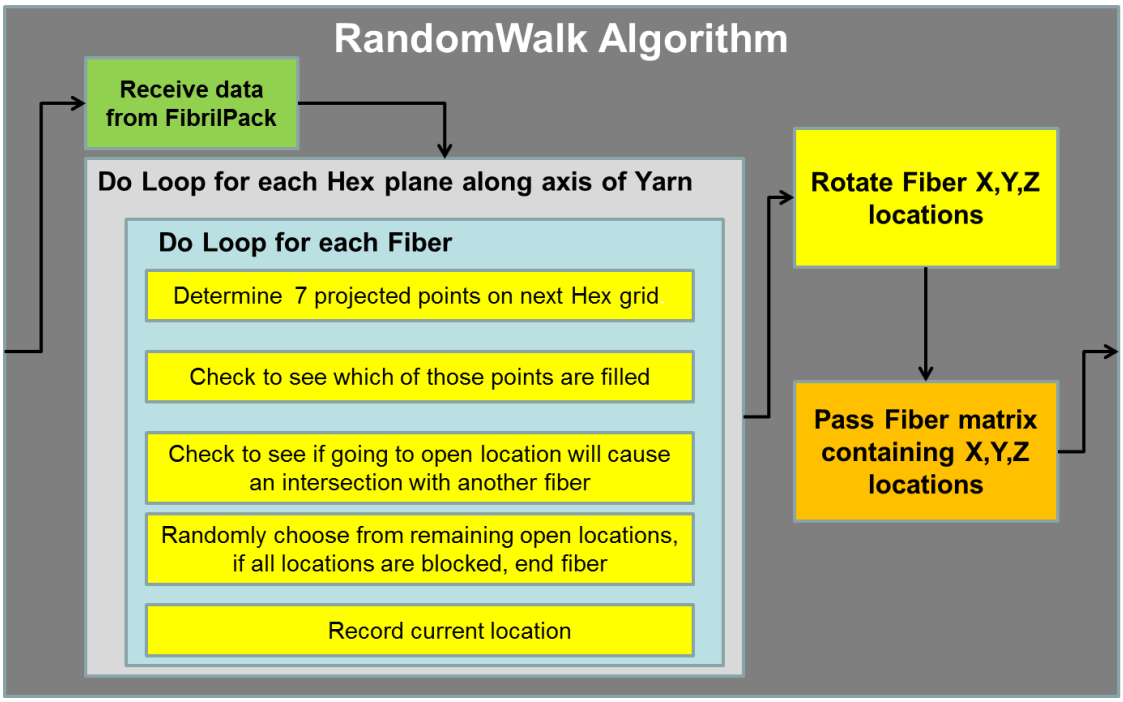

Figure 4.2 *Workflow of the pseudo code of the RandomWalk algorithm. The random prediction and overclosure checking is done inside a nested do loop for each fiber on each plane of the yarn. When the trajectories have been determined and rotated they are passed back to the FibrilPack program for geometry scripting.*

When these scripts are run in their respective programs, the geometry is created and automatically meshed. This methodology quickly creates a meshed geometry of complex woven filaments and allows for expeditious model creation, which for the geometry studied in this research was two hours, enabling the efficient attainment of the correct geometric parameters, as opposed to being burdened with redundant geometry creation tasks. An in depth description of the algorithm is presented in Ref. [16]. Analyses using the FiberWalk subroutine are able to capture the stress localization that is important to the final yield strength and modulus of yarn as seen in Figure 4.3.

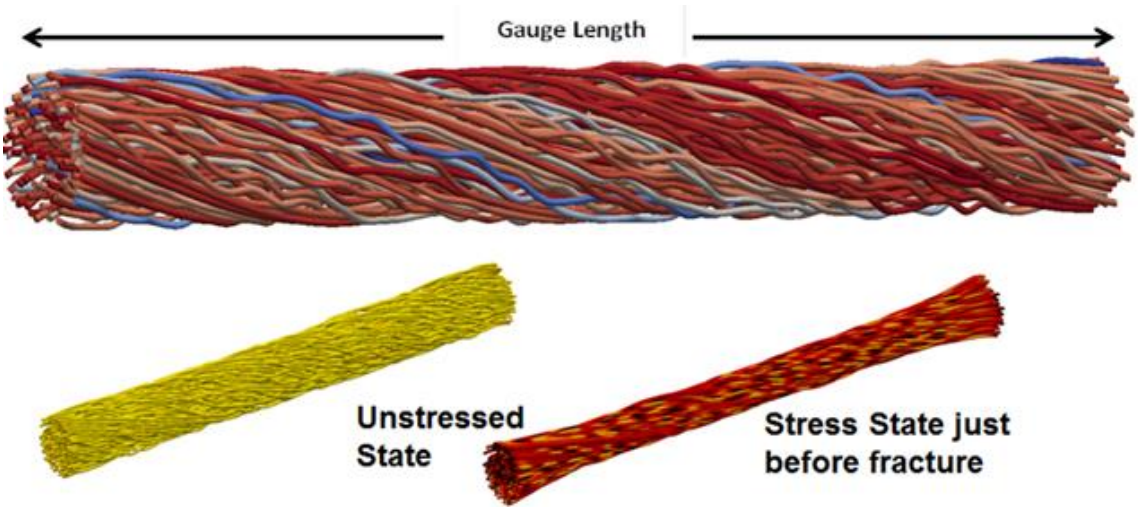

Figure 4.3 *RVE geometry (top) created by output of the RandomWalk subroutine. RVE comparison (bottom) between stressed and unstressed states. The stressed state indicates stress localizations (dark colored regions) due to intertwining of fibers.*

4.4.1 Kevlar KM2 Yarn Analysis

The hierarchy of Kevlar Yarn is a complex structure going from molecular bonds through fibrils and filaments and building up to a yarn. Thus constructing a model of even a simple yarn becomes a challenging RVE to create (see Figure 4.4).

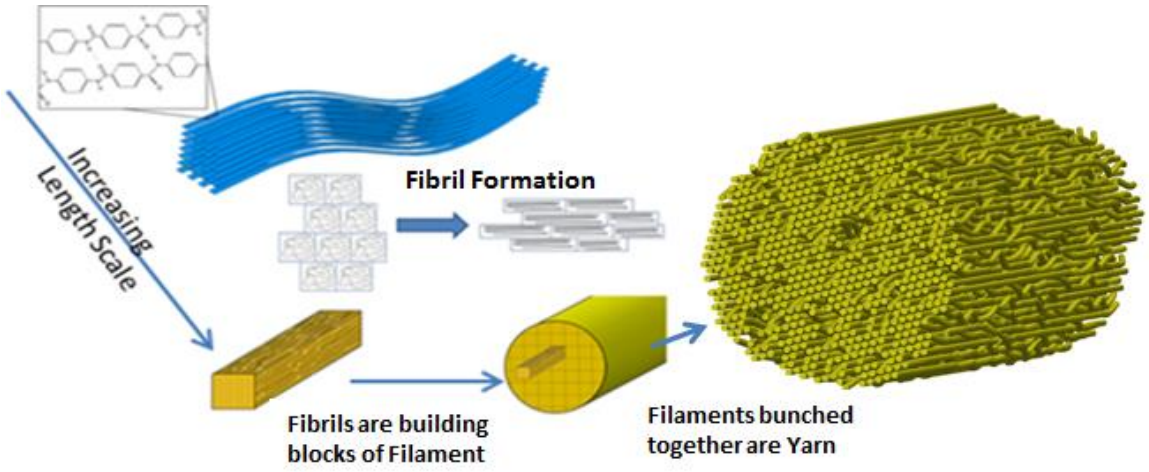

Figure 4.4 *Hypothesized Kevlar hierarchy developing from molecular bands to a filament with a micro-fibril based structure, while illustrating filament assembly to a straight yarn. Arrows denote increasing length scales.* ***[49]***

The purpose of this analysis is to reproduce the fracture strength of 600 denier Kevlar KM2 yarn of 588 fibers. For this analysis a filament was used as the lowest level building block. The representative yarn model was created knowing only the mechanical properties of the filament and the micro scale geometric properties of the yarn, namely, fiber diameter, yarn diameter, and number of fibers. The filament number was calculated dividing the cross sectional density of the yarn by the cross sectional density of the filament. The yarn gauge length for this analysis was 2.5 mm (Figure 4.5) because from the micrographs it was determined that this length allows the yarn to be composed of full length fibers, that is, there are no fibers ending within the yarn.

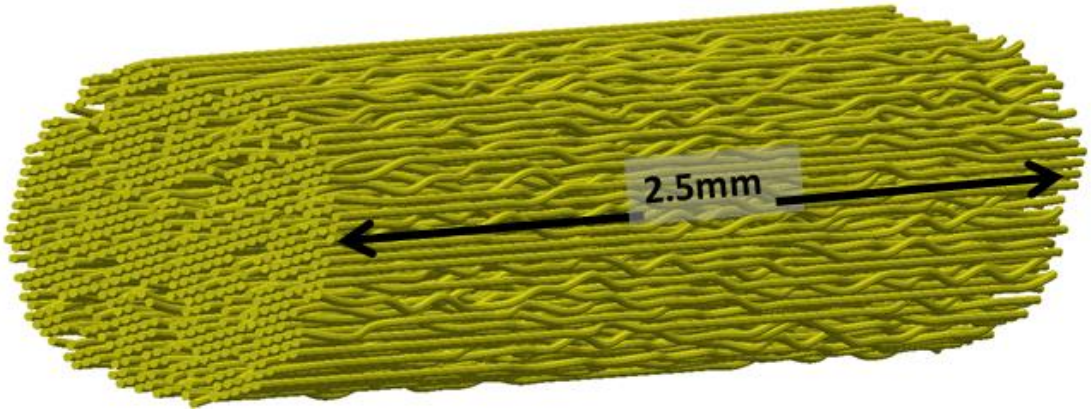

Figure 4.5 *A representative volume element (RVE) created for this analysis. 3D view of yarn length with intricate waviness and individual fibers and twist of yarn explicitly depicted.*

This simulation attribute was experimentally verified and enables the observation of the stress-strain distribution along the whole path length of a fiber. Figure 4.6 graphically illustrates filament interweaving and it an area where three filaments are switch positions creating an area of possible high stress concentration.

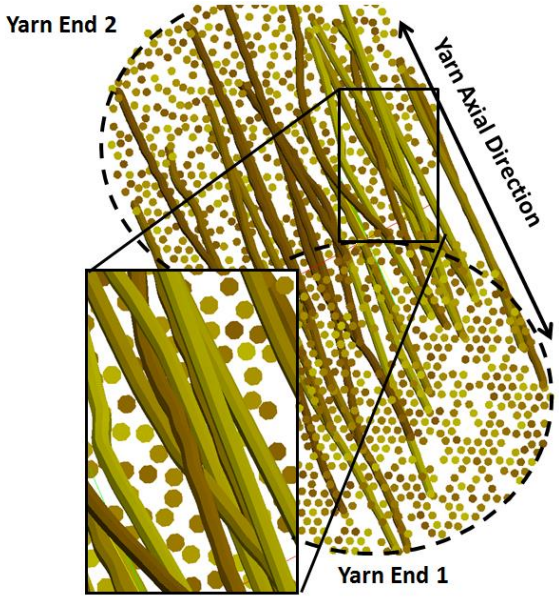

Figure 4.6 *Schematic depiction of geometric tortuosity and filament interweaving with their neighboring filaments. Circles indicate filament cross sections normal to their longitudinal axis. The various colors were chosen to highlight individual filament strands.*

The micrograph of Kevlar-KM2 yarn provides the filament diameter (10um) and yarn diameter (500um), as depicted in Figure 4.7. For Kevlar KM2 the ultimate strength is 3880MPa, the fracture strain is 4.6 (%) and 1.44 X 10^{-9} tonne/mm^3 density [5].

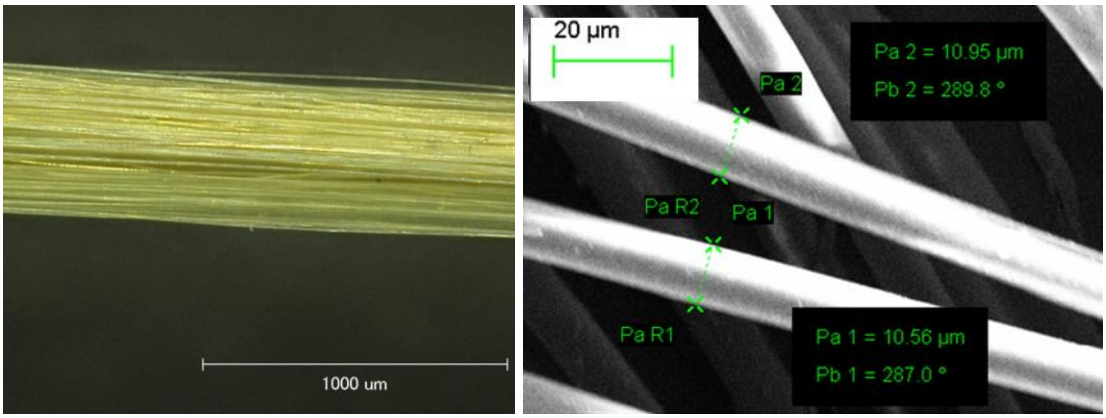

Figure 4.7*(Left) Micrograph of 600 Denier KM2 Kevlar yarn at x100 magnification; and (Right) SEM image measuring Kevlar KM2 filament.*

According to tensile tests previously conducted [5], the Kevlar filament undergoes brittle failure. Here, the Kevlar KM2 material properties were used to create a linear elastic fracture constitutive model to describe damage. In the future, a fibril/micro fibril level analysis can be used to create a more complex filament breakage constitutive relationship. The analysis was conducted using an explicit FEA solver using lofted beam hex elements [9]. Lofted beams were chosen due to their computational efficiency over standard hexahedral elements. Efficiencies were gained due to a decreased number of elements and an increased stable explicit time step. The beams lofted nature allows contact to be enforced with a given radial standoff keeping the geometry accurate. The solver was run over 0.00013 sec with a courant time increment of 1.5e-10s. During damage due to filament

breakage stress release wave motion is captured by the explicit solver and computed at each time step. Damage propagation due to acoustic wave motion is captured. A benefit of using an explicit solver instead of an implicit solution is the ability to assess damage progression of the individual fibers and its effect on the non-linear response of the yarn. A challenge of using this approach is that the boundary condition and solve time must be tailored to obtain a quasi-static twist and tensile pull before the failure point otherwise inertia of the fibers can influence the predicted elastic modulus.

4.4.2 Fiber Contact

The high complexity of fiber contacts in the model necessitates the employment of a general contact algorithm, as the manual handling of fiber contact pairs is inefficient. The Dash general contact algorithm was chosen because it is a face-to-face contact as opposed to a node to face method. The Dash contact algorithm encircles the beam axis with a lofted surface that is used only for the contact algorithm. A loft radius of 5um was assigned to each beam. This interaction has a coefficient of friction of 0.3. Friction is captured by the FEA model taking surface elements in contact and calculating the normal vector and force from the nodal forces of the surface element. The authors hypothesize that at less than 1 TPI the tortuosity of the fibrous structure is more significant to the resultant yarn force than fiber on fiber friction. The dependency on the friction coefficient is illustrated in Figure 4.8.

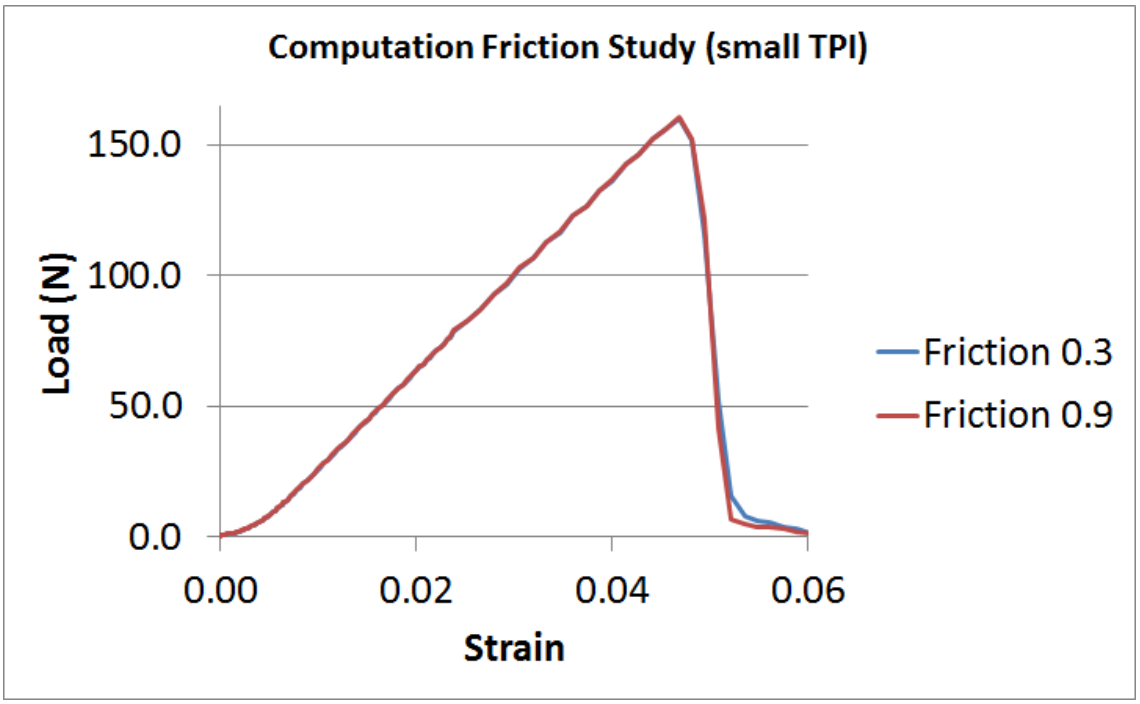

Figure 4.8 *Axial load versus applied strain for a 1TPI at two different frictional values, namely 0.3 and 0.9. The model exhibits minimal dependency to friction for this TPI*

Since the fibers are intertwined they tend to lock in place reducing the energy absorbed by the sliding fibers. This creates a small dependency on the friction coefficient. The tortuosity also reduces the effective gauge length of the fiber being pulled shown by stress localizations that are higher than the total yarn stress. Each fiber with a geometric localization absorbs a higher amount of energy than a fiber would with less entanglement. In the general contact algorithm all the fiber volumes are skinned (a surface set is created that includes all the outside surfaces of each fiber) for the face-to-face enforcement methodology. As the yarn is stretched during the analysis, the fibers are forced together due to the twist and random interweaving. The general contact keeps the fibers from overlapping and imparts the normal stress onto the contact faces.

4.4.3 Boundary Conditions

To predict the total yarn strength the RVE was analyzed in tension. The two ends of the yarn were held fixed in the transverse direction. This assumption is consistent with the clamps on a tensile machine trapping the ends and only allowing deflection in the axial direction. In the analysis the ends were pulled along the axial vector under a piecewise linear displacement boundary condition with a magnitude of 0.5mm. An analytical displacement rate boundary condition was employed to simulate a quasi-static pull. The goal was to displace slowly in order to gradually overcome fiber inertia effects then pull quickly to failure in order to optimize computational time. The solver calculates the force needed to create the prescribed deflection based on material properties, geometry and architecture of the yarn and the fibers.

Subsequent analyses were run to first preload the yarn with twist. The twist levels analyzed were 0, 3, and 10TPI. These twist per inch (TPI) values correlate to 0.0, 1.86, and 6.18 rad respectively. The calculation for these values is in the form of

$$Radians = (TPI) * 2 * \pi * Gauge \tag{4.1}$$

For the pre-twist simulations, the yarn was twisted using a smooth step piecewise linear curve that takes the form,

$$\beta = \frac{(t - t_i)}{(t_{i+1} - t_i)} \; for \; t_i \leq t \leq t_{i+1} \tag{4.2a}$$

$$a = A_i + (A_{i+1} - A_i) * \beta^3 * (10 - 15\beta + 6\beta^2) \tag{4.2b}$$

Equation 4.2b [56] defines the amplitude between points (t_i, A_i) and (t_{i+1}, A_{i+1}) for any time t. This equation has a small slope close to t_i and t_{i+1} with a larger slope in the middle

resembling an S curve. An example of the piece wise linear curve is shown in Figure 4.9. In the model, when the yard is twisted an axial load pre-load occurs if the boundaries are held fixed in the axial direction.

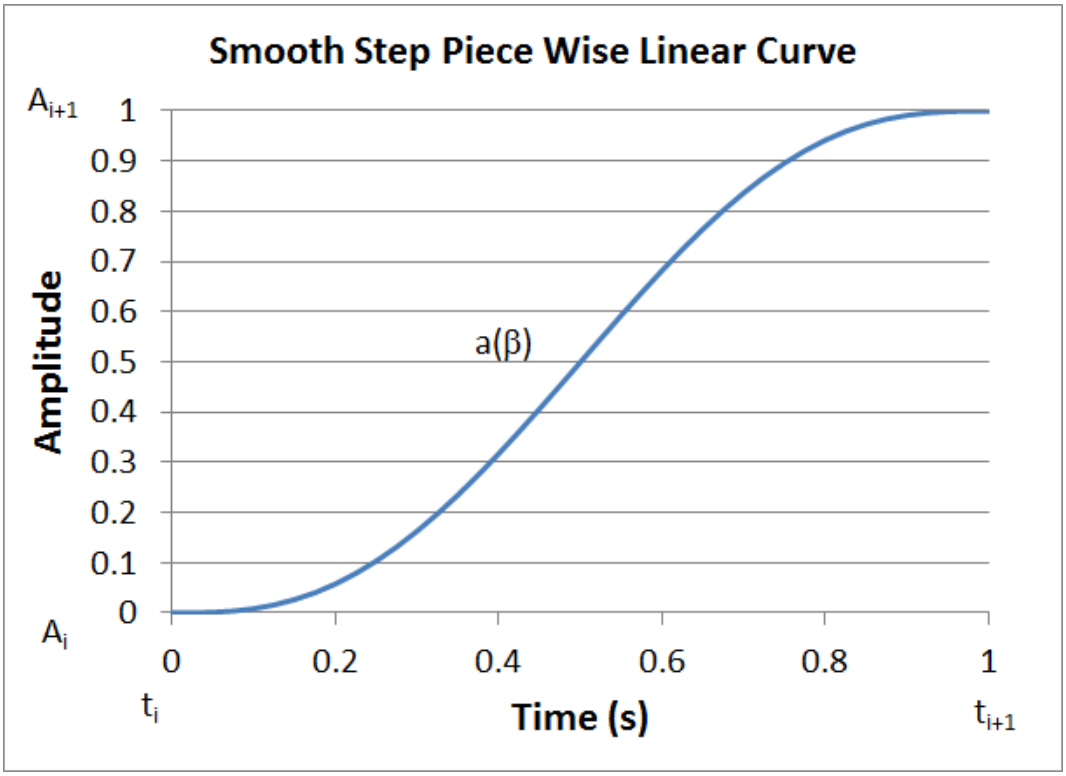

Figure 4.9 *Example of a smooth step curve as a function of beta. (β). Curve created from equations (4.2a) and (4.2b).*

An initial compressive offset was used to reduce the axial preload to a minimal value. The offset was deduced by iterating until the twist pre-load was less than 5N. An initial educated guess using the 0TPI case was used to minimize the iterations needed.

4.5 Results and Discussion

The yarn was subjected to an axial preload during the test and the analysis [48]. Without this preload it is difficult to get a uniform twist along the axis. The yarn's initial gain in strength as it is twisted to 3TPI and subsequent loss of strength as it progresses to 10TPI is attributed to the differential of strain from the outer yarns (higher strain values) to the inner yarns (lower strain values) due to the angular travel distance increasing with radius.

As the analysis progressed the yarn was stretched along the longitudinal axis. Initially, the response of the yarn was non-linear with a low stiffness. When subjected into tension the fibers pull tight against one another due to the twist. This creates local high stress nodes in the filaments that can absorb energy forcing the yarn structure to have a higher ultimate strength, see the stressed state in Figure 4.3. A time line of the yarn being twisted then failed is depicted for the 10TPI case in Figure 4.10.

Frame comparison between 0, 3, and 10TPI is illustrated in Figure 4.11. As seen, as the yarn is twisted it becomes more densely compacted along the transverse direction. During the pulling action, the outer filaments are stressed more than the internal ones.

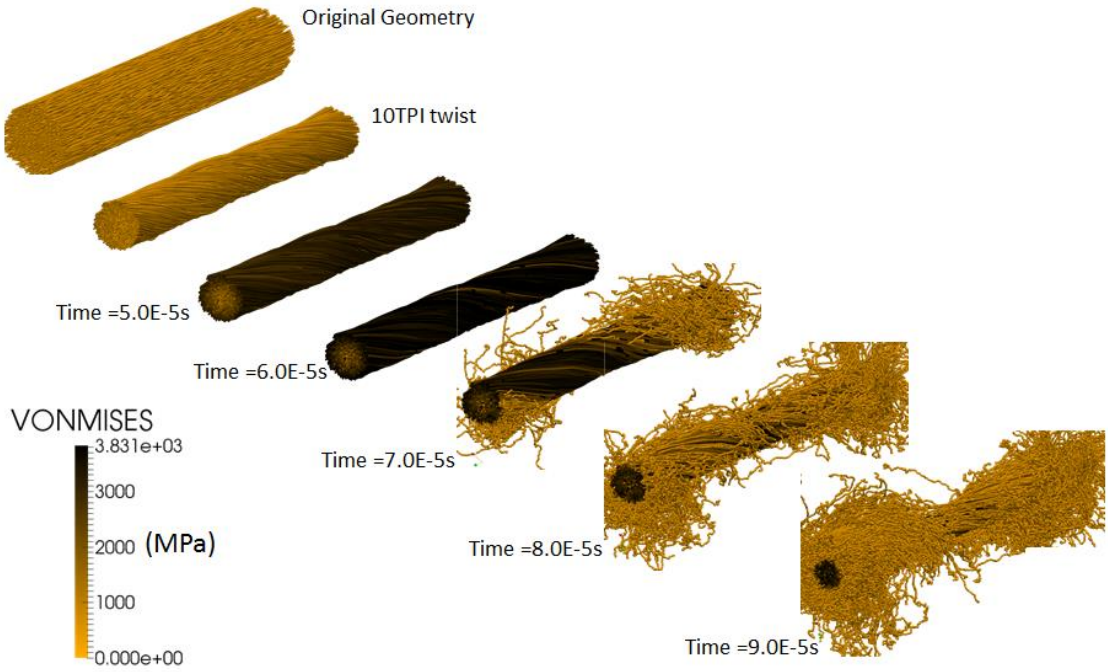

Figure 4.10 *Frames depicting timeline of twist and failure for 10TPI case of Kevlar KM2 yarn.*

This is due to a longer travel distance, owed to the arc length traveled during twist, to achieve the same axial strain that is associated with the twist amount. In addition, filaments that are interwoven create highly strained nodes. For these two reasons the failure point is most likely to occur on the outer yarn diameter at highly tortuous node. The figure shows that failure initiates on the outer diameter and grows inward.

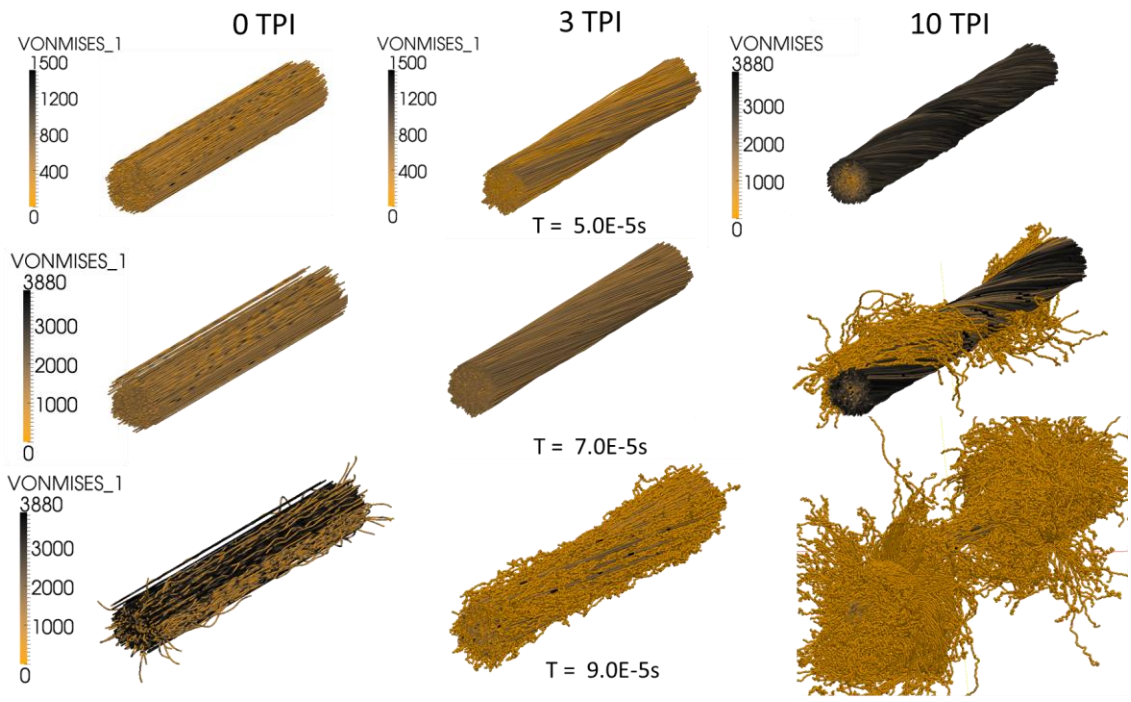

Figure 4.11 *Figure comparing axial load FEA of 600 denier Kevlar KM2 at various twist levels during initial twist (top) and eventual failure (mid, bottom). The 10TPI case fails first due to enhanced stress located in the outer diameter filaments due to twist.*

When the fiber is twisted beyond a certain point these high stress localities become strained reducing yarn stiffness and ultimate strength. Similar trends have been reported by X. L. Gao during axial pull to failure tests for Kevlar KM2. [48] The computational structural analysis results show the same trends seen during the tests. The predicted ultimate strengths at 0, 3, and 10 TPI match within 5% (Figure 4.12).

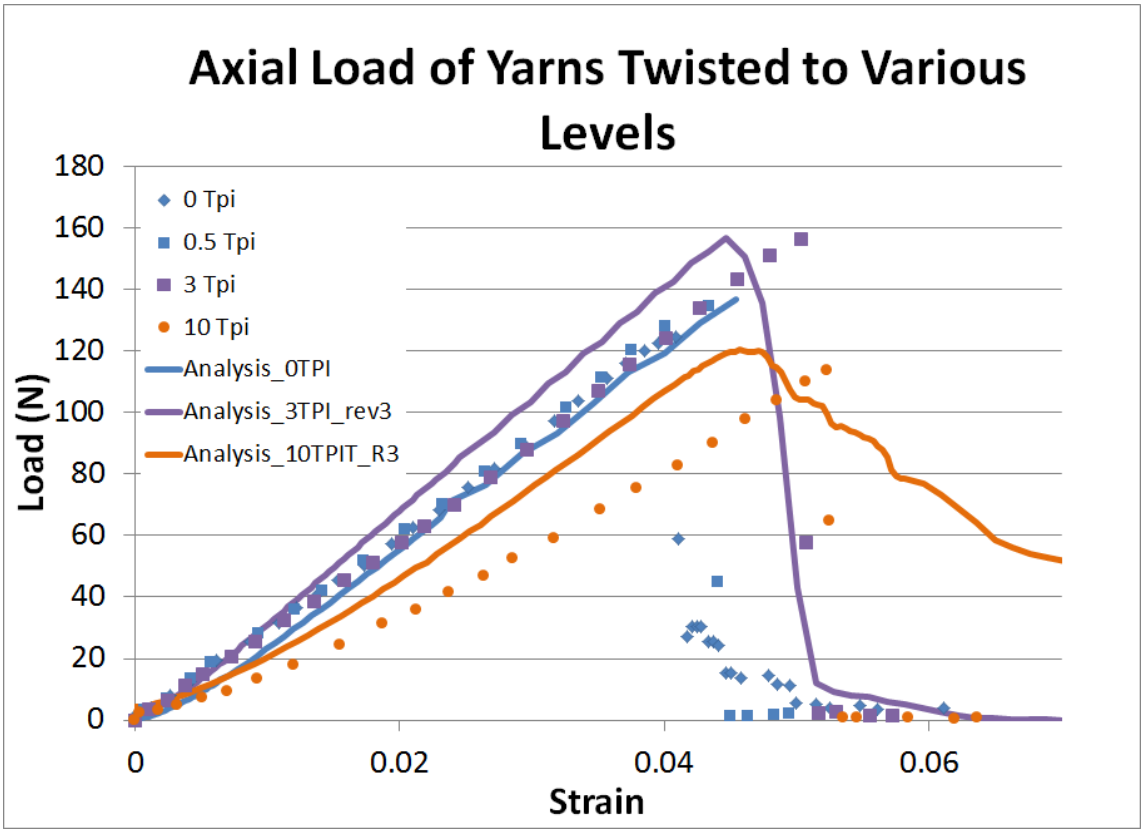

Figure 4.12 *Chart comparing axial load analysis of 600 Denier Kevlar to publish results at various twist levels. The failure stress predicted by the analysis is within 6% of the published values.*

The predicted yarn stiffness matched within 5% at 0. The 3 and 10TPI computational model stiffness was within 17% from that observed in the test. since the initial portion of the load versus strain chart is highly non-linear, the compared stiffness values were taken from the part of the curve located between 0.03 strain and the failure strain for each curve. A notable disparity between the tests and the computational model was observed to be in the non-linear portion of the yarn response. It is hypothesized that including the filament breakage variance as a randomly applied failure point for each part in the analysis would improve the computational models fit to the test results; nevertheless, this point is of future research interest and outside the scope of this paper.

4.6 Conclusions

The generated 600 denier Kevlar KM 2 multi-scale computational model was twisted to 0, 3, and 10TPI and consecutively was pulled under tensile load until failure. The model correlates to macro scale, namely 600-denier yarn, experimental results based on only micro scale (filaments) geometry and Kevlar properties. Computationally there was little dependency of the yarn response to friction observed. When the model was pulled to failure the predicted ultimate load was within 5% for all three twists per inch analyzed. The predicted linear response fit within 17% for the 3 and 10TPI cases. The 0TPI linear response matched to within 5%. To enhance the computational model the non-linear portion of the load response curve has to be improved upon. It is proposed that including the statistical deviation of the filament stiffness and strength values would improve the predictions the computation model can provide. The modeling used for geometry creation and failure can predict yarn strength as a function of twist and filament geometry.

Since damage initiates on the outer yarn filaments, different approaches to increase the yarn strength by twisting past 3TPI may be considered. One course of action to improve functionality would be to create a variable twist as a function of yarn radius. In this manner, the inside yarn will be spun higher than the outside reducing the outside stress. Alternatively, the outside of the yarn may be treated with a flexible urethane that slightly increases the failure strain. The FEA models built can aid in providing valuable insight in the selection of these methods for increasing overall yarn strength before complex tests are commenced.

4.7 Acknowledgements

The authors kindly acknowledge the financial support PEO-Soldier of the United States Army Contract W91CRB-12-P-0047 P00003 to perform this research.

Chapter 5 : Tenacity Dependence of Twisted Kevlar Yarn

5.1 Abstract

Kevlar KM2 600 denier yarn is often twisted to improve yarn load at failure. It is noted in ASTM-D-7269 that twisting KM2 past five twists per inch can cause a lower load at failure. Understanding the physics that govern the load decrease at higher twist ratios can lead to improved yarn designs, possibly stronger than the peak values currently seen at three turns per inch. Increasing yarn strength would enable enhanced usage of Kevlar yarn, improving chord and fabric structures. This paper describes the testing and finite element analysis methods used to probe yarn tenacity as a function of twist per inch. The performed tests indicate that strength decreases as the yarn is twisted past three twists per inch and are in agreement with previously conducted tests. The finite element model results were compared to sets of test data performed in this study and ones reported in the literature. Employing the validated simulation data, yarn damage and failure pictorials were produced. The frames showing the yarn at varying displacements illustrate the yarn failure propagation at varying twist-per-turn values. It is suggested that yarn softening as a function of twist per turn is attributed to higher strains of the outer filaments, at large amounts of twist, than the core filaments. Previous work has shown a dependency of local filament strength to its yarn radius. [1] The focus of this paper is to derive a comprehensive filament model, using finite element analysis that incorporates the yarn strain gradient and is experimentally verified.

5.2 Keywords

composites, fiber, fracture, Kevlar, KM2, micro fibrils, multiscale simulations, nanostructure, para-aramid, aramid, twist, TPI

5.3 Introduction

Twist is the most common practice for improving para-aramid yarn performance amidst methods that include strategic material selection, enhanced composite yarn design, and enriched molecular structure of fibers [57, 58, 59, 60, 61]. The ability to predict yarn tenacity dependence on twist is critical for design engineers since optimization of yarn strength and weight for specific systems, such as tire chord or fabric design, requires predictive simulation tools [62]. It has been observed that yarn strength increases up to 3 twists per inch, and decreases with further increase of the TPI value [63, 8, 64, 65, 66]. The research in this paper construes and models the behavior of yarn strength as a function of applied twist. Experiments are performed to reproduce previously published trends of yarn strengthening and subsequent weakening with increasing twist. To capture important physics of yarn damage at the yarn filament level, a representative volume element (RVE) model for the yarn is created, and further employed, to predict the structure's damage behavior at 0, 3, and 10TPI.

The experiments were conducted at the Advanced Materials and Structures Laboratories (AMSL) at Rutgers University following the ASTM-D-7269 standard [8]. In order to perform testing to that standard, a new grip for holding the yarn was machined and installed on the 1kN Instron. Testing was conducted at the machine setting suggested by the ASTM. The yarn was preconditioned for 3 hours at 45 deg C, 15% relative humidity

(RH) and conditioned for 14 hours at 20 deg C, 64%RH per standardized procedures. Previous work has shown that near room temperature the statistical tenacity range is less than 5% [67]. Deviations from the obtained results and previously reported data from the Gao [63, 64] are attributed to discrepancies between manual and automatic yarn twisting, and in cross head speed calibration between testing equipment. The maximum load dependency, first strengthening then weakening, to TPI observed by AMSL is similar to the trends observed in Refs [63, 1, 68, 65, 66].

To probe the acquired results and applicable physics of yarn breakage an RVE that could replicate the witnessed trends is developed. Fabric and yarn properties such as tenacity and load at failure are captured in custom made RVEs [69, 32, 70, 34, 71, 54, 6, 32, 70, 34] The cited research spans from the micro (atomistic) to macro (weave) length scales. However, studies at the yarn and weave scales ignore yarn tortuosity and twist although an important part of creating predictive RVEs at larger length scales compels inclusion of Kevlar filament-to-filament interaction attributed to tortuosity. Randomly oriented and intertwined filament micro-geometries necessitate the structure of an RVE in which a fiber is randomly entangled with its neighbors. A method of random axial filament projection is employed to create yarn geometry of interwoven filaments. This type of geometry describes the initial yarn state more accurately than a parallel filament assumption [16]. The approach taken in this paper projects the fibers along one direction mirroring what happens in natural processes such as tissue generation. Projecting fibrous microstructures along a direction simplifies the algorithm proposed by Altendorf [35], in which rectangular shape is filled with spheres and then multiple splines are fit projected from one sphere center to the next until the rectangle is filled. Recchia et al. [16, 46]

developed a method at AMSL, which gives up randomness in one direction so that the model is able to create cylindrical fibrous structures. These structures are applicable for building yarns, cables, and bundled geometries. The RVE is analyzed using the Sandia National Labs structural mechanics solver Sierra [9]. This code is chosen because it can handle lofted beam elements in its general contact algorithm. Sierra's parallel computing time also linearly scales up to 1 million processors.

In this paper, the above-mentioned procedures are followed to reproduce the experiments and enhance the investigation with a parametric study. Visualizations from the data and the RVE simulations agree with previous research that twist can be the damage mechanism resulting at lower maximum loads at failure for the 10TPI case [72]. A model that can estimate the damage seen in the FEA is derived that calculates a maximum TPI of a yarn when its filaments are assigned threshold values of strain that is based on their strain at failure [5].

The model derived through this research holds true for yarn cross sectional areas that are circular. When a yarn is chorded or put into a weave there is an additional strain component added to the pre-load of the structure [69]. This research describes the first step to building a constitutive model based on filament properties and is valid for structures consisting of a single yarn.

5.4 Tensile Tests and Grip Design

In order to probe Kevlar KM2 yarn tenacity dependence on twist per inch (TPI), tensile tests were conducted at 0TPI, 3TPI, and 10TPI. New grips dedicated to fiber loading into

an Instron 4411 (1 kN capacity) were machined and assembled according to ASTM-D-7269. [8] The yarn fixture is illustrated in Figure 5.1.

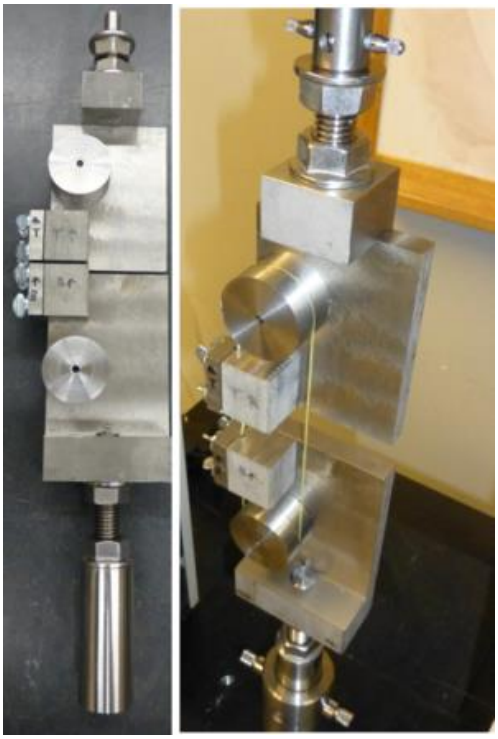

Figure 5.1 *The AMSL grip design attached to the Intron tensile machine. The yarn is gripped on top then passes through 180^0 rotation in the hemispherical grooves on the top cylinder. It passes through another 180 deg. rotation on the bottom cylinder and is gripped on the bottom. The minimum gauge length that can be tested by this design is 10 inches.*

The fixture mounts to an Instron material testing system through upper and lower shear pins. The cylinders contain a hemispherical groove to align the yarn. The clamps have a female V groove and male V notch. The yarn length was 23 inches, was routed between the two grooved cylinders, and clamped by the grips. Both sides of the clamping notch were coated with a high friction rubberized plastic. Since Kevlar has been shown to be highly strain rate dependent [73], the appropriate TPI, as stated in Ref. [8], was applied by pulling the bottom shear pin and twisting the bottom clamp to achieve the twist per inch desired. The twist was done with enough slack in the yarn to ensure no pre-load. To further

establish that no preloading ensued, the load output was carefully monitored while twisting took place. If any load greater than 1lb while twisting was detected by the load cell the crosshead was lowered to prevent preloading. However, the yarn was held taut enough that it never left the centering grooves in the upper and lower cylinders to ensure perfect alignment. The yarn was tested at 0, 3, and 10TPI. The load versus displacement data was recorded electronically. The tests were conducted using ASTMD7269 [8] guidelines, indicating cross-head speed of 10 in/min and gauge length of 15 inches. This corresponds to the gauge length used in previous research probing Kevlar's statistical dependency on fabric location and gauge [3] Twenty-five specimens were tested at 0TPI, and 15 specimens were tested at each 3 and 10TPI cases.

5.5 Test Results

Each yarn specimen was loaded into the grips and pulled through failure. A minimum of 15 tensile specimens was pulled for each twist per inch value, while ensuring that failure occurred within the gauge length. The 0, 3, and 10TPI AMSL test results were compared against data taken by Gao [63].

The data of the performed 0TPI experiments are illustrated in Figure 5.2(a) while in Figure 5.2(b) the minimum, maximum, and mean values of the test specimens were plotted in blue.

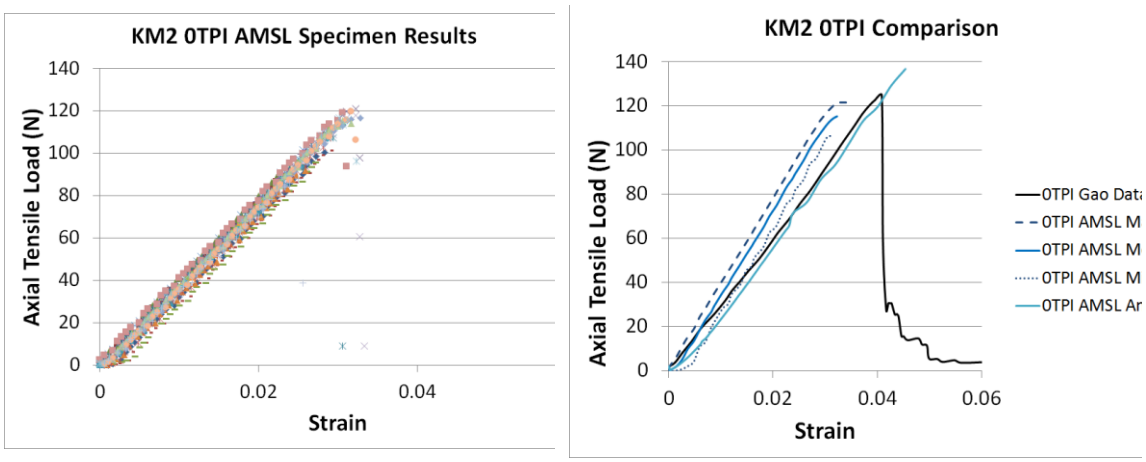

(a) **(b)**

Figure 5.2*(a) 0TPI tensile test specimen results (b) The minimum, maximum and mean values of the test specimens were plotted in blue. The black line is 0TPI data taken from tests conducted by Gao **[63]**. The AMSL load at failure matches within 8% to Gao's data and 18% to the analysis.*

The black line shown is 0TPI reference data from Gao [63]. The tested stiffness matches to the stiffness seen in the referenced data. The mean AMSL peak load at failure matched within 8% to the Gao load at failure.

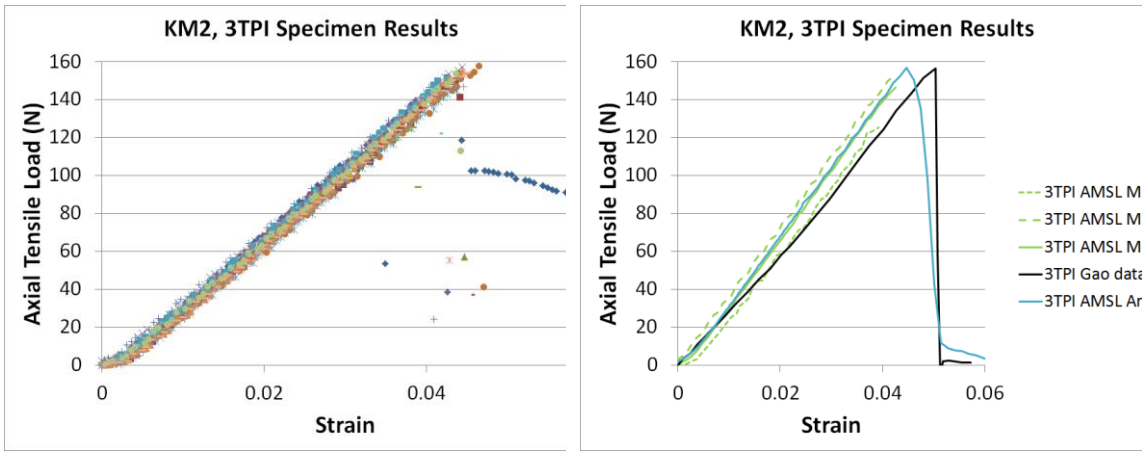

(a) **(b)**

Figure 5.3*(a) 3TPI tensile test specimen results (b) The minimum, maximum and mean values of the test specimens were plotted in green. The black line is 3TPI data taken from tests conducted by Gao **[63]**. The AMSL load at failure values match within 7% to Gao's data and 7% to the FEA simulation.*

In Figure 5.3(a) the results from the 3TPI tensile test specimens are presented. A total of 15 specimens were compared. Figure 5.3(b) illustrates the minimum, maximum

and mean values of the AMSL 3TPI results plotted in green. The black dotted line is 3TPI data as reported by Gao [63]. The AMSL load at failure values matched to the Gao loads within 7%.

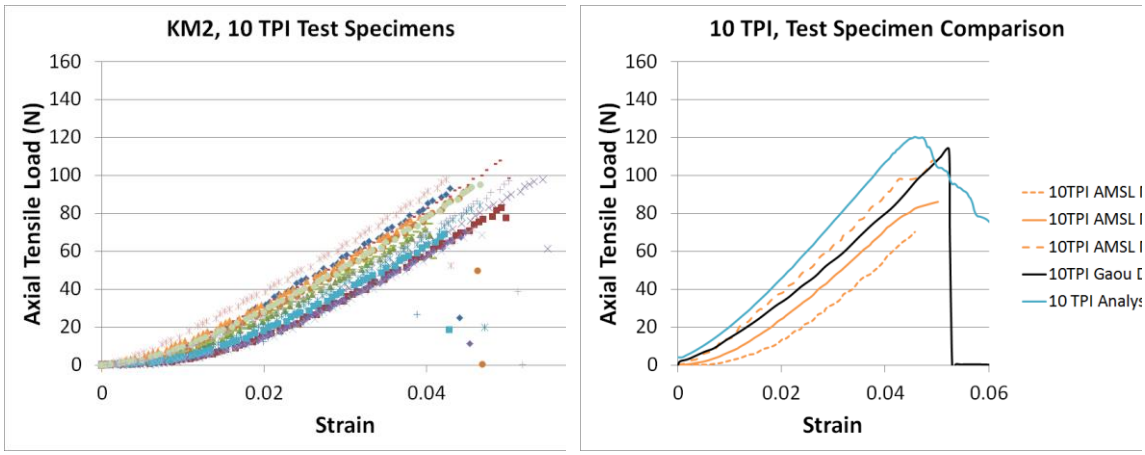

(a) **(b)**

Figure 5.4 *(a) 10TPI tensile test specimen results (b) The minimum, maximum and mean values of the test specimens were plotted in orange. The black line is 10TPI data taken from tests conducted by Gao.* ***[63]****. The stiffness becoming lower as twist increases from 3TPI to 10TPI is captured in Gao, AMSL tests and the AMSL FEA model. There is a large dispersion in the results for the 10TPI tests. This is due to hand twisting the samples. The AMSL test specimens that failed at a higher stress match well to the results from Gao and the FEA model.*

The 10TPI AMSL tensile test specimens results are depicted in Figure 5.4(a) while Figure 5.4(b) illustrates the minimum, maximum and mean data values plotted in orange. The black line indicates the Gao 10TPI data. The stronger maximum load specimens match well to the referenced data (within 5%). For 0, 3 and 10TPI the AMSL data falls short of the Gao [63] reported data. This is most likely due to the grip design or the method used to impart the twist on the yarn. The current design of the test fixture allows for free yarn length between the two centering discs, see Figure 5.1. The ASTM standard calls gauge length, which is presumably the free length, the length between the centering discs augmented by the length of the quarter arc of the two discs.

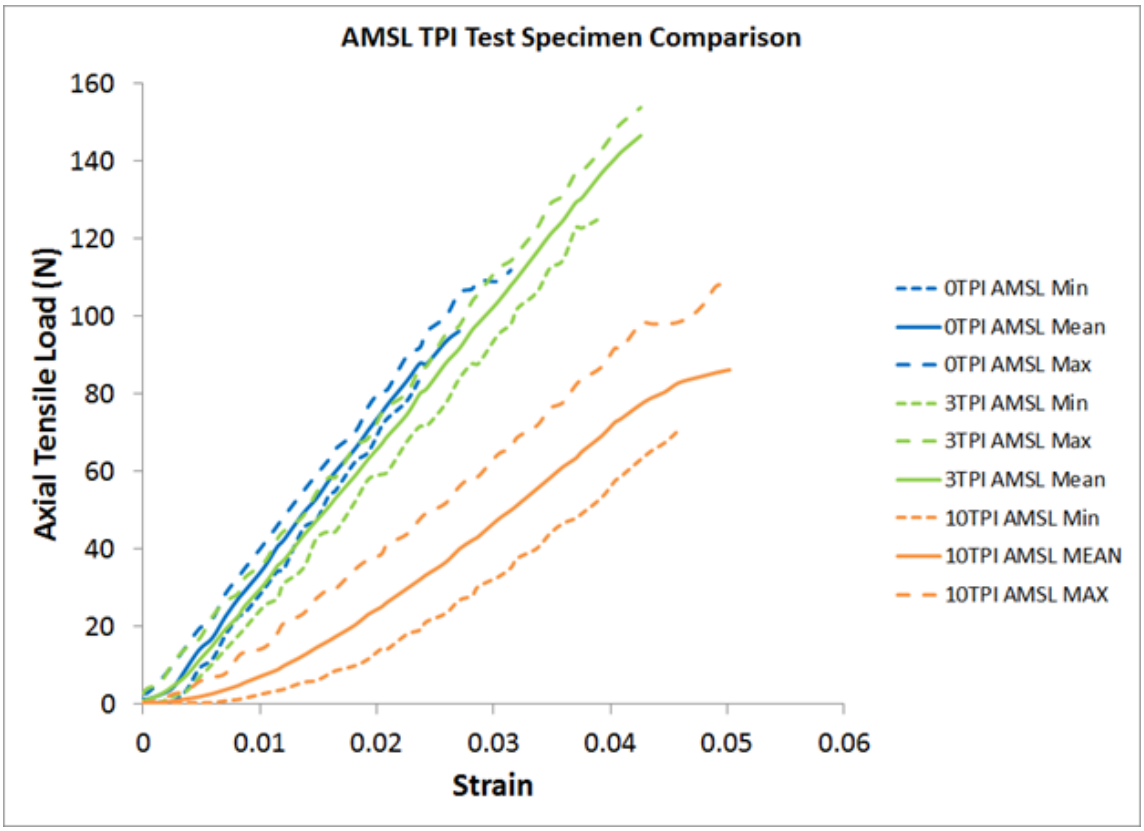

Figure 5.5 *(a) 0TPI, 3TPI and 10TPI AMSL test results were plotted for comparison. The data indicate that yarn tenacity increases from 0-3TPI and decreases from 3-10TPI.*

A comparison of all AMSL test results, namely 0, 3, and 10TPI, are plotted in Figure 5.5. The data depict that the yarn tenacity increases from 0-3TPI and decreases from 3-10TPI. For the 0TPI and 3TPI cases the stiffness values do not change. The 10TPI specimens illustrate a lower stiffness than that of the 0-3TPI specimens. It is hypothesized that the same principles that apply to lower the load at failure trigger the lower yarn stiffness. To determine what instigates the load and stiffness change, a finite element analysis (FEA) is employed to probe the filament interaction within the yarn.

5.6 Kevlar KM2 Yarn Analysis

To investigate the response of the twisted yarn failure an FEA model was developed for the 600 denier KM2 yarn [23, 16]. The AMSL tensile specimens and Gao data [63] are compared to the AMSL finite element model in Figure 5.6. The yarn stiffness between the FEA model and the tests agree within 17%. As twist increases the response of the yarn becomes non-linear and the corresponding stiffness becomes a harder metric to gauge. The load at failure of the FEA matches the referenced data well within 5%.

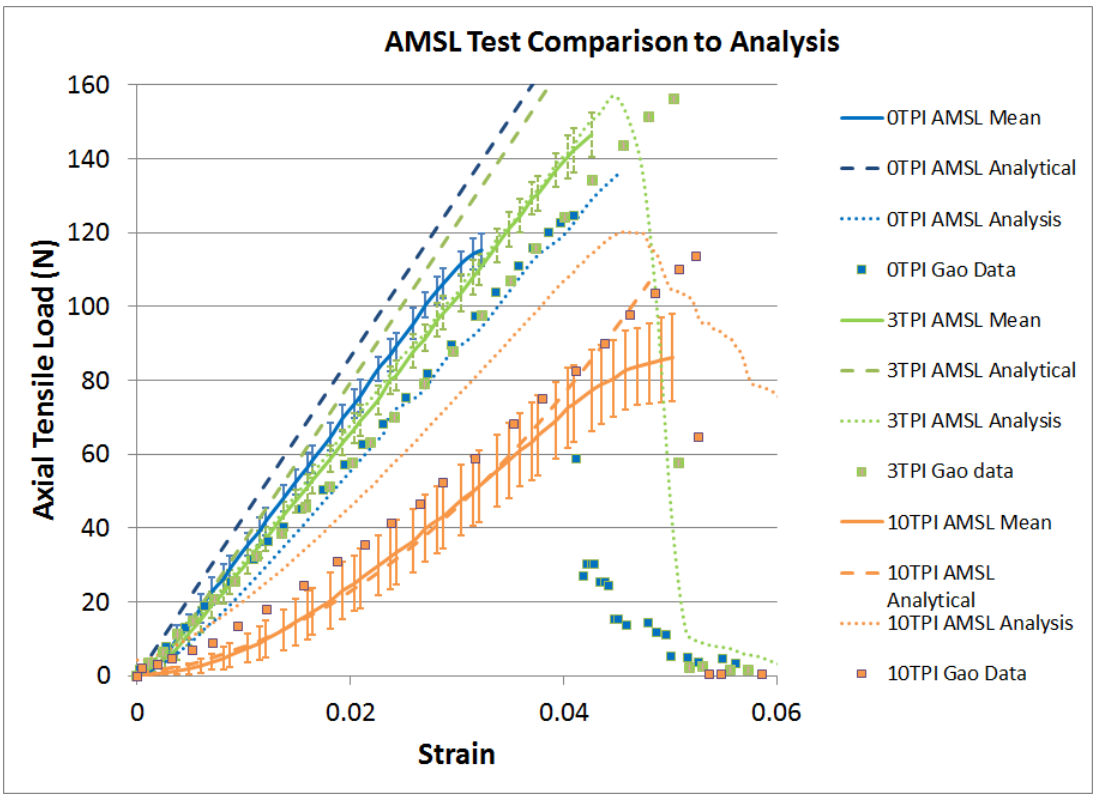

Figure 5.6 *The AMSL tensile specimens and reference data **[63]** are compared to the FEA analysis. The AMSL test error bars are based on standard deviation seen during testing. The yarn strengthening and weakening as a function of TPI trend is seen in the two tests and the analysis. Since the physics of yarn load at failure as a function of twist is capture in the FEA. It is possible to derive an analytical model that captures the same physics as the FEA for predicting yarn failure.*

The load at failure predictions for the 0TPI case is 136N. The AMSL mean value recorded is 115N and the maximum load at failure recorded is 121N. For the 3TPI case, the FEA predicts slightly higher load at breakage 157N compared to the mean tested value of 146N. When the finite element model is compared to the maximum load seen in the specimens, namely 153N, the data compares within 3%. For 10TPI the model predicts a failure load of 120N, the AMSL tests recorded a mean value of 86N and a maximum value of 107N.

The FEA model does not capture precisely the initial non-linear load versus strain response of the 10TPI test specimens. To highlight the intricate procedures the twisted yarn experiences at failure the progressive yarn damage through strain increase for 0, 3 and 10TPI are illustrated in Figure 5.7.

Figure 5.7 *Figure comparing axial load FEA of 600 Denier Kevlar KM2 at 3 and 10TPI. The plot shows the variation of initial (unstretched) stress state at the two twist values. The 10TPI case fails first due to enhanced stress located in the outer diameter filaments due to twist.*

The simulations in the figure feature the difference in yarn initial state between the 3 and 10TPI cases. The initial stress due to twist for 3TPI appears homogeneous with high stress localizations due to filament tortuosity. The 10TPI initial stress plot indicates that the outer filaments are strained to a much larger extent. The outer filaments start out within 10% of the filament breakage strength (3880MPa). This causes a difference in the yarn failure between the 0 and 3TPI case, and the 10TPI case as shown in the middle and bottom rows. For the 0 and 3TPI, the yarn breaks at points throughout the yarn diameter. The breakage points are due to areas where tortuous filaments create high stress nodes in the yarn. As damage progresses the breakage remains distributed throughout the length and cross section of the yarn. For the 10TPI twist, the higher stressed outside filaments are the first to break and damage progresses from the yarn's outer diameter and proceeds inward.

5.7 Analytical Yarn Model

There is a need for an analytical model that can predict yarn strength based on TPI. Researchers have tried to come up with an empirical model that captures the strength dependence on twist. The model proposed by Rao [1] illustrates the strength dependency but not the stiffness change. It is also empirically based on yarn data and not dependent on filament properties. In contrast, this paper describes a physics-based method for predicting failure strength and yarn response by evaluating filament strain in layers throughout the yarn. The FEA yarn model is successful at predicting the strength at failure for a twisted yarn. The analytical AMSL yarn model uses the same physics and boundary conditions as the FEA model. The measurable quantities applied in the formulation of the FEA model

are denoted in Table 5.1 and are implemented to derive filament and yarn properties employed in our analytical equation.

Table 5.1 *Table of measurable filament and yarn properties*

Measurable Filament and Yarn Properties						
Term	Yarn Denier (g/9000m)	Filament Modulus (GPA)	Filament Density (g/cm^3)	Filament Diameter (μm)	Gauge Length (mm)	Filament Strain at Breakage
Symbol	Den	E_f	ρ_f	D_f	L_g	ε_{fail}
Value	600	84.62	1.44	10	250	0.0452
Derived Filament and Yarn Properties						
Term	Filament Area (mm^2)	Filament Cross Sectional Density (g/m)	Yarn Cross Sectional Density (g/m)	Filament Count	Close Packed Yarn Area (mm^2)	Close Packed Yarn Radius (mm)
Symbol	A_f	X_f	X_Y	N_{fil}	A_Y	r_Y
Equation	$A_f = \frac{\pi {D_f}^2}{4}$	$X_f = \rho_f * A_f$	$X_Y = \frac{Den}{9000m}$	$N_{fil} = \frac{X_Y}{X_f}$	$A_Y = \frac{N_{fil} A_f}{0.906}$	$r_Y = \sqrt{\frac{A_y}{\pi}}$
Value	7.854E-5	0.0001131	0.06667	589	0.0511	0.1275

Development of the finite element model necessitates assignment of an elastic constitutive model with brittle filament fracture to a lofted truss element. The element deletion occurs at 0.0452 strain as discussed in Cheng's work [5]. The same stress response is used for the analytical model. The FEA model indicated that there is a stress and strain gradient between the outside and the inside of the yarn when twisted above 3TPI, see Figure 5.7. For this reason, the stress is evaluated at 15 separate levels throughout the radius of the yarn.

The yarn is numerically divided into 15 layers where each layer is a column in a matrix. The strain, stress and force can be evaluated in each layer separately. The force in each layer is summed as shown in Figure 5.8 to give the yarn force response to elongation.

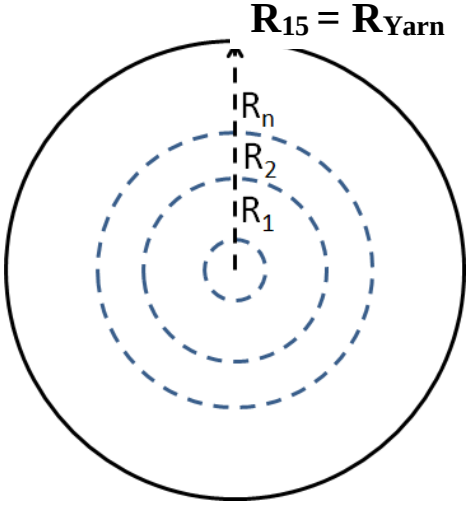

$$A_n = \pi(r_n - r_{n-1})^2$$

Evaluated

for n = 1. . 15;

Where: $r_0 = 0$

$$F_{Yarn} = \sum_{n=1}^{15} E_f \varepsilon_n A_n$$

Figure 5.8 *Diagrams depicting cross section of yarn split into layers, showing how the force of each layer is summed into a total yarn force. The mechanical response is akin to a system of parallel springs, where each layer is represented as a spring.*

This method breaks the yarn into separate load paths that resemble a system of parallel "springs". By evaluating each layer individually the proper layer (radius) dependency on twist can be applied to the model.

It is expected that the 0TPI case will have the same filament strain throughout the yarn's cross section as the yarn is loaded. For any twist above 0TPI there will be a shifted filament strain due to twist for each yarn layer. The shifted filament strain due to TPI is a

function of yarn twist, angle, and radius. The yarn twist angle, α, and pre-strained filament length, H, are calculated as shown in Figure 5.9.

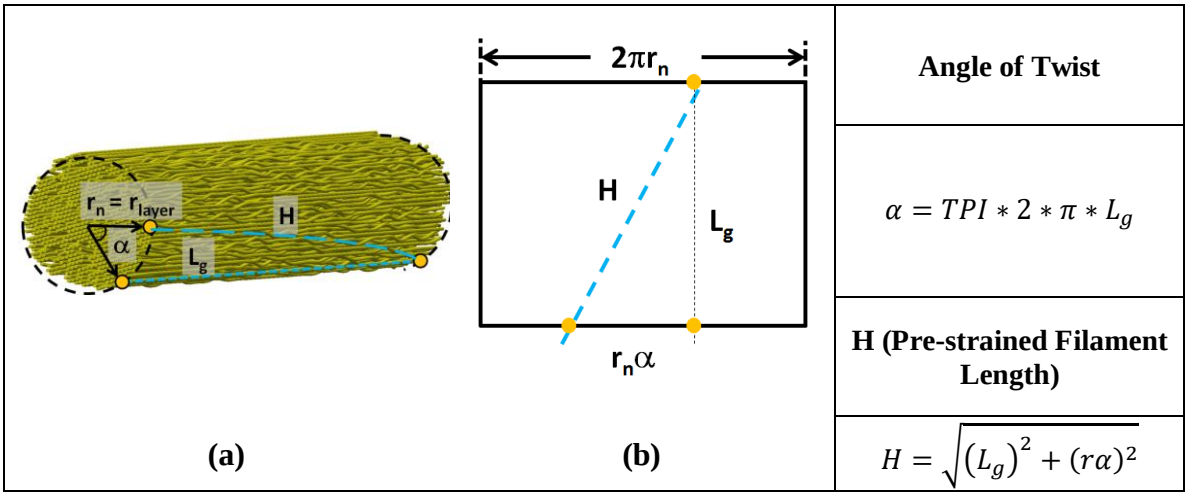

Figure 5.9 *Diagrams depicting filament projection along a twisted yarn and calculation of pre-strained filament length due to twist.*

The equations stated in Figure 5.9 are applicable when the ends of the yarn are held fixed during twist. It is noticed that when this boundary condition is used in the FEA simulation, the force versus strain response is shifted due to a pre-load being applied by the twisted strained filaments. Referring to ASTM-D-7269 [8], when testing yarn under twist, the yarn is kept at a constant force, not displacement. To account for this boundary condition Equation 5.1b is modified with a Δ_{pre} to account for the relaxation due to constant

summed force being held less than 2N. The displacement imposed due to tensile pull is also accounted for in Equation 5.1b as Δ.

$$H = \sqrt{\left(L_g + \Delta\right)^2 + (r\alpha)^2} \tag{5.1a}$$

$$\varepsilon_{Layer} = \varepsilon_n = \frac{\sqrt{\left(L_g + \Delta - \Delta_{pre}\right)^2 + (r_n\alpha)^2} - L_g}{L_g} \tag{5.1b}$$

Equation 5.1b is evaluated at each of the 15 layers of filaments along the radius. Each layer has a corresponding filament strain to yarn displacement, Δ. The shifted strain is used to calculate the corresponding stress using the filament's young's modulus. The stress in each filament layer is used to calculate the layer's force. The force on each layer is summed and plotted versus yarn strain. These values are compared to the published data in Ref. [63].

Since the yarn force response to elongation has been thus far derived from known geometry and filament properties, the poor fit observed in the tests of Figure 5.10 was initially intriguing.

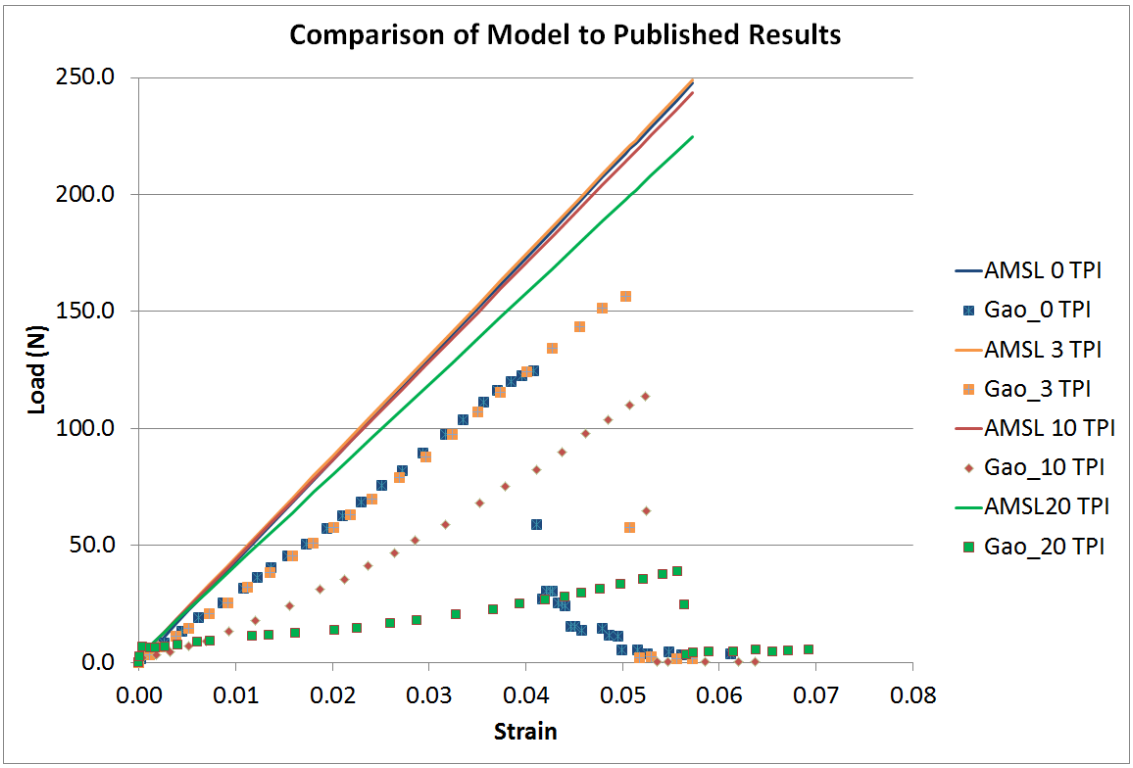

Figure 5.10 *Comparison of analytical summed layer force to published **[63]** test of twisted KM2 yarn at four different twist levels. All of the predicted forces are much higher than any of the test data. This solution of the equation cannot reproduce load as a function of twist.*

When the values for layer axial force are examined, the inner layers are subjected to axial compression. Nevertheless, the filaments cannot undergo axial compression from negative displacement of the cross heads, while maintaining a constant load. The filament geometry dictates that buckling would occur during axial compression and give a “wet noodle” response, during which the axial negative displacement is stored by the filament buckling and must be overcome by yarn elongation before that layer becomes part of the load path.

The idea that a filament cannot go into compression changed the analytical model by adding in a command, which evaluates that if a strain is negative then a zero value is imposed for that data point. When this statement is added to the analytical model, the relaxed displacement due to the constant force boundary condition is increased. With this

new addition the axial displacement for 3, 10, and 20TPI became 0.001, 0.012 and 0.055mm respectively.

Once the assumption that filaments cannot hold compression is made, the analytical model agrees with the test data. It is noted that the 10 and 20TPI cases contain many zero points for small strains during loading (< 0.03). As the displacement increases, the number of layers in the yarn subjected to tension increases. This clarifies the issue of a filament with an elastic brittle behavior exhibits a non-linear response when put into a twisted yarn as seen in Figure 5.11.

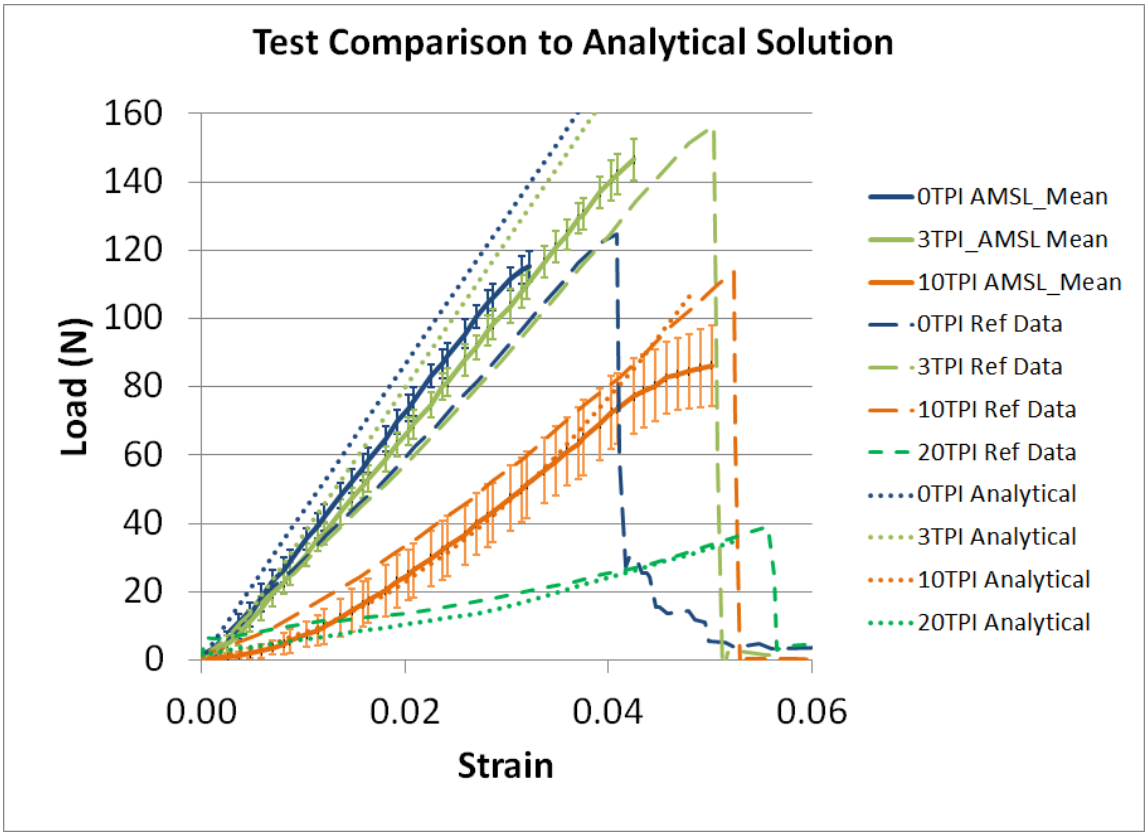

Figure 5.11 *Comparison of analytical equation to AMSL tests and published experimental data Gao **[63]**. The AMSL test error bars are based on standard deviation seen during testing. The modulus softening is seen in the two experiments and analytical solution. The increase then decrease in load at failure seen during the tests is reproduced by the analytical solution.*

The suggested methodology indicates that yarn strengthening is caused by a larger failure strain due to twist. Yarn weakening is attributed to the total length decrease attained when a yarn is twisted at a constant axial force. The closer a filament is in the outer perimeter of the yarn the larger the distance it has to travel, see Figure 5.9. Since the yarn has to be subjected to constant load the twisting action imposes a larger strain on the outer filaments compared to the inner ones which travel a smaller distance, and which remain relative unstrained. The decrease in yarn length causes the inner filaments to refrain from carrying any load initially. This implicit reduction of yarn filaments in the load path reduces the overall stiffness resulting in lower failure loads. Figure 5.11 illustrates the yarn's force dependency on twist ratio is produced by this analytical solution. Next, a method for predicting a yarn breakage strain is developed. For the twisted fiber, the strain in the outer filaments is larger than the yarn strain. Therefore, the layer with the largest strain is located on the yarn's outer diameter. An adjusted yarn failure strain can be calculated by using Equation 5.2.

$$\varepsilon_{Yarn\,Fail} = \frac{\sqrt{\left(\varepsilon_{fail}L_g - L_g\right)^2 - (r_{Yarn}\alpha)^2} - L_g + \Delta_{pre}}{L_g} \qquad (5.2)$$

where ε_{fail} is the filament breakage strain and ε_{yarn_fail} is the predicted failure strain for the yarn. Equation 5.2 is obtained by substituting the failure strain into Equation 5.1b and solve for the yarn displacement. The yarn displacement is used to calculate yarn strain by dividing by the gauge length. Using this method the failure strain is predicted based on

yarn twist angle, yarn close packed radius, and relaxation due to twist force. The predicted failure strains are plotted on Figure 5.12.

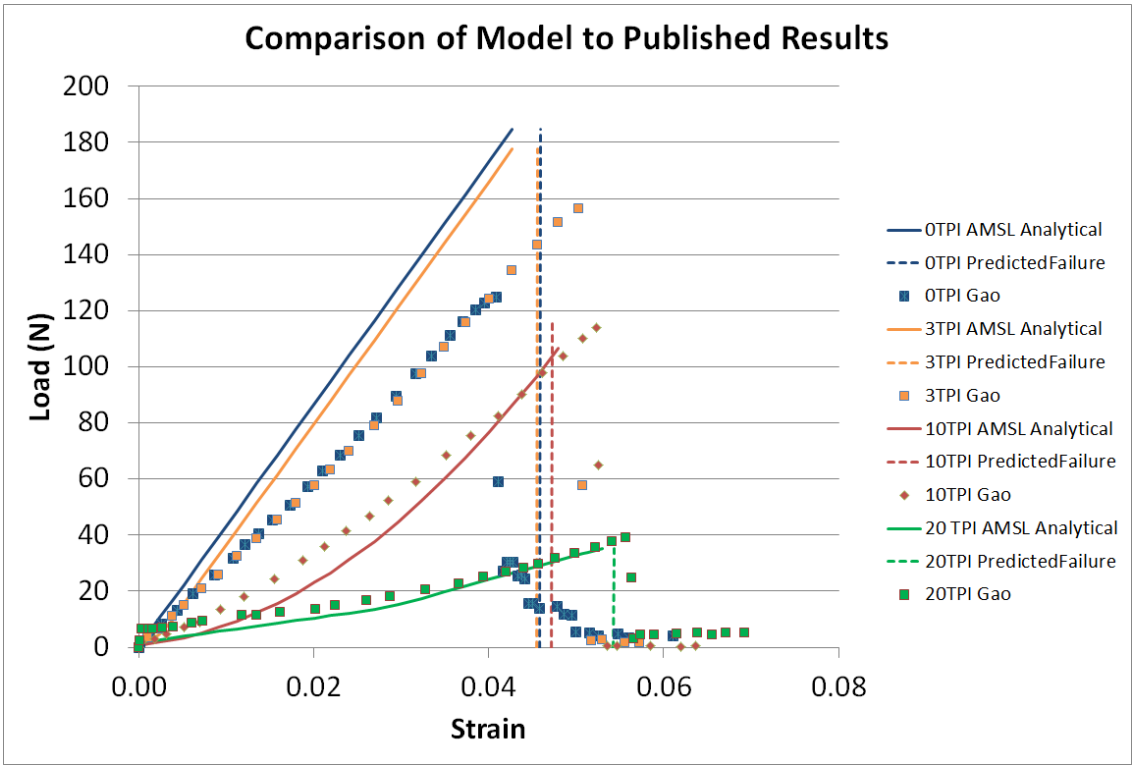

Figure 5.12 *Predicted failure strain calculated by Equation 5.2. For all the cases the strain at failure predicted is below what the tests showed* ***[63]****. The trend of larger failure strain at higher twists is reproduced by the analytical solution.*

This methodology captures the increased strain of failure for the 10 and 20TPI cases while it does not produce a difference in the failure strain for 0 and 3 TPI cases. The increase in failure strain for the 3 TPI case is an area for further research.

5.8 Discussion of the Analytical Model

The predicted failure strains increase as the twist is increased which is seen in the AMSL yarn tests as well as in the published values in Ref. [63]. The Rutgers AMSL yarn

equation, can predict the yarn's strength dependency on twist up to 20TPI. This methodology is based on filament linear elastic mechanical properties and determination of local strain due to geometry, and is not sensitive to friction. To evaluate the latter statement, finite element simulations where performed for friction values of 0.3 [46] and 0.9 in which the yarn modulus did not significantly change in the results. For this reason friction was not used when creating the analytical solution.

The yarn moduli for the 0 and 3TPI cases are higher by a factor of 1.28 compared to the results published by Gao [63]. It is hypothesized that the tortuous path existing along the yarn may cause the deviation in modulus. A plot showing the prediction with a shifted modulus is shown in Figure 5.13.

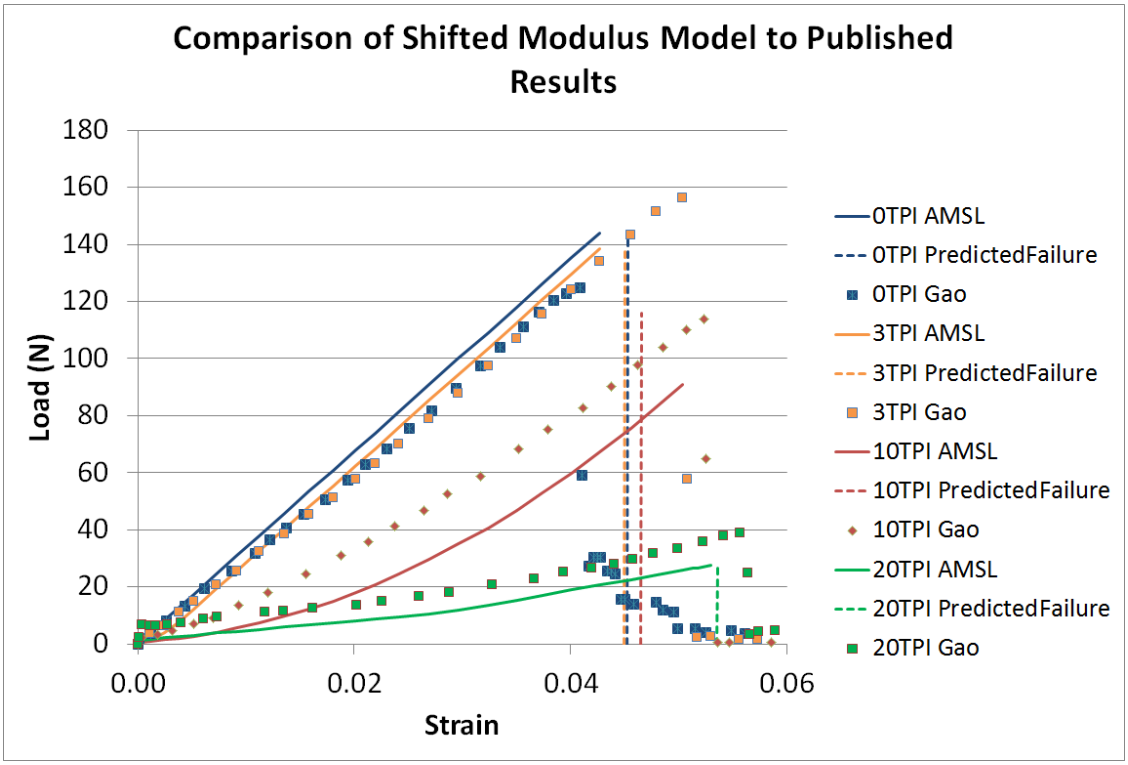

Figure 5.13 *Strain Failure prediction using shifted yarn modulus. The results follow the same trend as the data. The 0 and 3TPI cases match closer than the unshifted modulus case but the 10 and 20TPI cases are farther away. The failure strain is lower than the tested values.*

The results follow the same trend as the test data. The 0 and 3TPI cases match closer than original analytical solution but the 10 and 20TPI cases are also shifted. Since the 10 and 20TPI responses are more dependent on the outer yarn filaments, it is presumed that the larger strains the outer filaments undergo suppress the inherent tortuosity effect of the individual filaments, which is more pronounced in lower TPI ratios.

The predicted failure strain can be modified to account for elongation due to radial compression. The failure yarn strain, Δ_{fail}/L_{gauge}, can be numerically calculated through iterating elongation until ε_{fail} is equal to the filament failure strain 0.0452 [5].

$$\varepsilon_{Fail} = \varepsilon_{n=15} - \varepsilon_{shift} \tag{5.3}$$

$$\varepsilon_{shift} = \frac{\sigma_{radial} * \gamma_{12}}{E_{12}} \tag{5.4}$$

where ε_n is evaluated at the outside yarn radius and ε_{shift} is the strain elongation due to radial compression. The ε_{shift} is based on transverse Poisson's ratio and transverse modulus. The radial stress is equal to the cross sectional pressure divided by 2. The cross sectional pressure is derived from hoop stress of the outer most layer. The pressure is calculated from the thin wall cylinder approximation $P = \frac{\sigma_{hoop} * t}{r_{yarn}}$. The thickness of the layer is assigned the filament diameter d_f. The hoop stress is equal to the hoop strain, ε_{hoop}, multiplied by the filament elastic modulus, E_{33}. The hoop strain component is equal to the hoop component of the strain. By following the above procedure and performing the appropriate substitutions Equation 5.4 becomes Equation 5.5, as indicated below:

$$\varepsilon_{shift} = \frac{\varepsilon_f * \cos\tan^{-1}\frac{L_g + \Delta - \Delta_{pre}}{r_{yarn} * \alpha} * E_{33} * d_f * \gamma_{12}}{2 * E_{12} * r_{yarn}} \tag{5.5}$$

By substituting Equations 5.1b and 5.5 into Equation 5.3 we obtain Equation 5.6:

$$\varepsilon_{fail} = \frac{\sqrt{(L_g + \Delta - \Delta_{pre})^2 + (r_n \alpha)^2} - L_g}{L_g} - \frac{\varepsilon_f * \cos\tan^{-1}\frac{L_g + \Delta - \Delta_{pre}}{r_{yarn} * \alpha} * E_{33} * d_f * \gamma_{12}}{2 * E_{12} * r_{yarn}} \quad (5.6)$$

Yarn failure, Δ/L_{gauge}, is calculated by iterating Δ until ε_{fail} is equal to the filament failure strain. Figure 5.14 depicts the predicted yarn failure strain values at each twist rate.

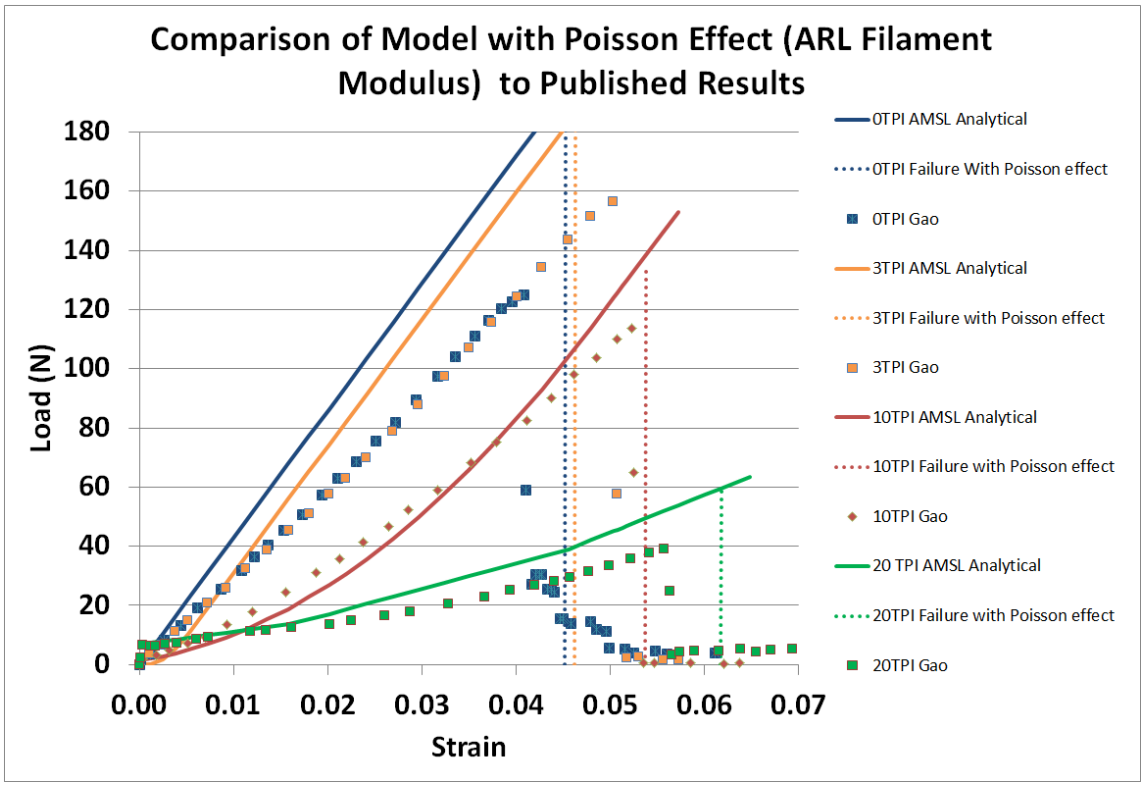

Figure 5.14 *Analytical model evaluated Tusit's (ARL* ***[5]****) reported filament modulus (84.3 GPa). The failure strain predicted was modified to incorporate filament elongation due to radial stress from twist, Poisson's ratio and filament modulus. Filament failure strain, Poisson's ratio and transverse modulus are taken from ARL's report to be 0.452, 0.24 and 1.34GPa respectively.*

The analytical model evaluated with the shifted Poisson's failure strain based on Ref. [5] reported filament modulus of 84.3 GPa, see Figure 5.14. The predicted failure strain was modified to incorporate filament elongation due to radial stress from twist, Poisson's ratio and filament modulus. Filament failure strain, Poisson's ratio, and transverse modulus are reported with values of 0.452, 0.24 and 1.34GPa respectively [5]. When testing filaments Gao measured a slightly different filament modulus [63] than the data in Ref [5].

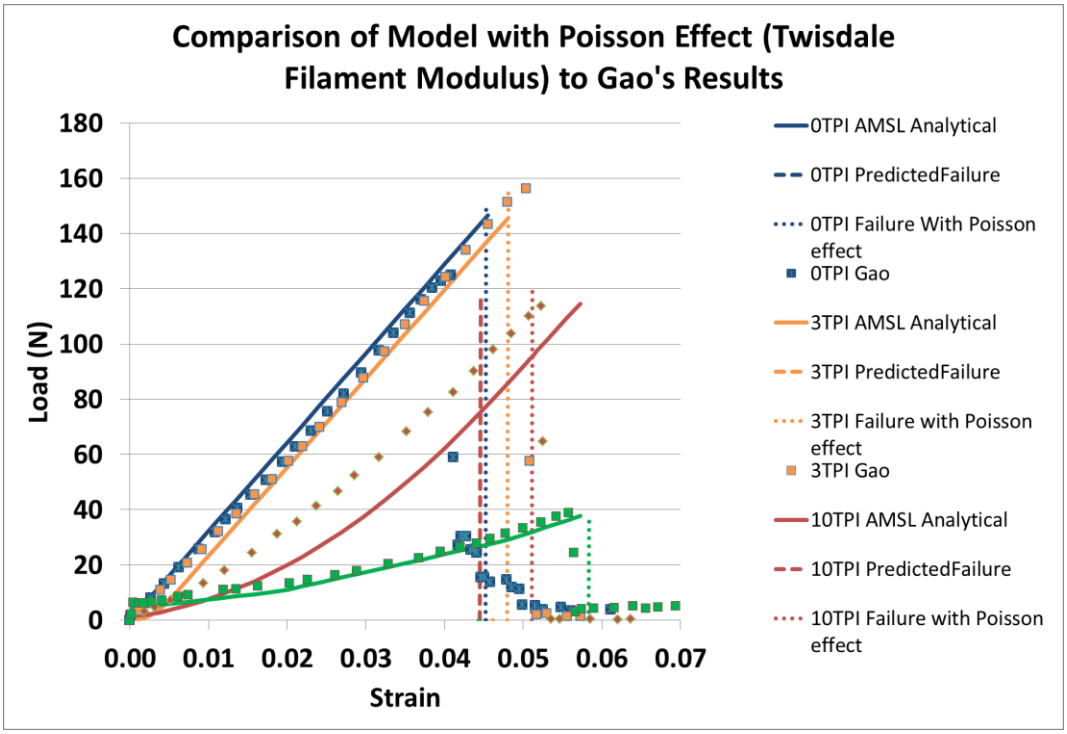

Figure 5.15 *Analytical model evaluated with Twisdale's reported filament modulus* **[74]** *(63 GPa). The failure strain predicted was modified to incorporate filament elongation due to radial stress from twist, Poisson's ratio and filament modulus. Filament failure strain, Poisson's ratio and transverse modulus are taken from ARL's report to be 0.452, 0.24 and 1.34GPa respectively.*

Figure 5.15 illustrates the analytical model evaluated using the filament modulus of 63 GPa reported by Twisdale et al. in Ref [74]. The failure strain predicted was modified to incorporate filament elongation due to radial stress from twist. By using the Twisdale's

filament modulus in the AMSL analytical model a close fit to the reported (Ref. [63]) yarn data has been generated. The yarn failure strain curves from AMSL tests, FEA, and analytical solution are compared to the published data [63] in Table 5.2.

Table 5.2 *Comparison of the AMSL yarn failure varied by twist to Gao's published data* ***[63]***.

	0 TPI	**3TPI**	**10 TPI**	**20TPI**
Gao's average failure strain	0.041	0.0507	0.0511	0.0605
AMSL analytical failure strain	0.0458	0.0455	0.047	0.0543
AMSL Analytical failure strain with Poisson Effect (Twisdale Filament Modulus)	0.045	0.048	0.051	0.058
AMSL analytical failure strain with Poisson Effect (ARL Filament Modulus)	0.045	0.049	0.054	0.062
AMSL Average Tested Strain at Failure	0.0322	0.0425	0.0502	***N/A***
AMSL FEA Model Prediction	0.045	0.044	0.045	***N/A***

The analytical model using the filament modulus measure by Twisdale; matched the published average failure strain [62, 74] from the yarn tests closely when the Poisson's effect was taken into account. The AMSL tests showed the same trends in yarn failure strain as Gao's but had lower strain values. The FEA analysis did not account for yarn failure strain changing with twist. This is due to the execution of the analysis with truss elements so no transverse compression was allowed and thus had no Poisson's effect.

5.9 Conclusions

In order to probe tenacity of 600 denier Kevlar KM2 as a function of TPI grips compliant with ASTM-D-7269 were fabricated and installed on a 1kN Instron 4411

universal testing apparatus. The results obtained from 600 denier Kevlar yarn tensile tests at 0, 3, and 10 twists per inch conducted at AMSL compared well to tests conducted by Gao [63]. The AMSL mean load at failure values were lower than the Gao tests for 0, 3 and 10 twists per inch values tested. The maximum values seen throughout testing matched well to the literature reported values [63]. One possibility for the load at failure difference between AMSL data and published d data in Ref. [63] was the manual twisting of the yarn. This may lead to an inconsistent preloaded strain condition throughout the yarn cross section. The initial strengthening, then weakening of maximum yarn load was observed as a function of TPI in both the AMSL and Gao test results. In order to visualize important physics of yarn stretch and damage an FEA model was created to predict failure for the 3TPI values of interest.

The FEA showed that the initial pre-stress state of the yarn changed between 0, 3 and 10TPI. In the 0 and 3TPI case, there was no strain gradient between the yarn's center and its outer diameter. In the 10TPI case the filaments on the outside of the yarn were strained almost to breakage, where the filaments on the inside (close to center axis) were not. This behavior is attributed to the fact that filament strain was derived as a function of TPI and radius. To reproduce the load at failure dependency on twist, this equation is evaluated over every layer within the yarn and the filaments are not allowed to undergo axial compression (strength set to zero). The model predicts the linear to non-linear transition of the load response to elongation due to increasing twist. The yarn failure strain can be predicted reasonably well for the 0TPI, 10TPI and 20TPI case by the analytical model. The yarn failure strain equation does not capture the strain increase for the 3TPI case, even though the FEA was able to capture that phenomenon. The only physics

included in the FEA that was missing from the analytical model is the tortuous path of the filament through the yarn. The FEA and the analytical model predict that the twisted yarn will always fail at the outer filaments as is observed in our experiments. By incorporating the Poisson effect into the yarn failure strain calculation. The AMSL solution was closer to the tested values at all twist values.

One should note that the analytical solution results presented here are geometry dependent, therefore this type of calculation is insufficient to be used if the yarn is part of a weave or chord. In that case the yarn's cross section is deformed from its original circular shape. An additional strain due to the applied boundary condition can be added to obtain the appropriate yarn failure strength and strain for those specific fibrous structures such as those created by Zhou [69]. By building an analytical equation that incorporates the physics from the finite element model that was able to mimic the yarn tenacity as a function of twist ratio, a method for predicting yarn tenacity based on yarn denier, filament geometry and filament mechanical properties has been developed, tested, and verified.

5.10 Acknowledgements

The authors kindly acknowledge the financial support PEO-Soldier of the United States Army Contract W91CRB-12-P-0047 P00003 to perform this research.

Chapter 6 : Conclusions

6.1 Kevlar KM2 Yarn Model Correlation

The developed 600 denier Kevlar KM2 representative FEA model was twisted under constant axial force to 0, 3 and 10TPI. After twist was applied the geometry was pulled until tensile failure occurred. The model correlates to experimental results based on only micro scale geometry and filament properties. Computationally, there was little dependency of the yarn response to friction observed. When the model was pulled to failure the predicted ultimate load was within 5% for all three twists per inch analyzed. To improve the computational model the non-linear portion of the load response curve has to be improved upon. The derived analytical solution showed much better correlation to 10 and 20TPI than the FEA model. It is proposed that by making the filaments unable to hold compression, thus becoming a “wet noodle”, the finite element model will match the linear to non-linear load response. The modeling tools used for geometry creation can be used to reproduce any yarn like structure including ring spun yarn. Using this FEA methodology the strength dependency on twist can be predicted based only on microscale filament properties.

6.2 Tensile Testing of Kevlar KM2 Yarn

The AMSL mean load failure values were lower than the Gao [48] tests for 0, 3 and 10 twists per inch values tested. The maximum values seen throughout tested matched well to the UT reported values. The load at failure difference between AMSL data and Gao data is most likely due the AMSL grip design and twisting mechanism. The initial

strengthening, then weakening of maximum yarn load was observed as a function of TPI in both the AMSL and Gao [63] test results. In order to visualize important physics of yarn stretch and damage an FEA model was created to predict failure for the 3TPI values of interest.

6.3 Analytically Derived Model

The FEA showed that the initial pre-stress state of the yarn changed between 0, 3 and 10TPI. In the 0 and 3TPI case, there was no visible strain gradient between the yarn center and yarn OD. In the 10TPI case, the filaments on the outside of the yarn were strained almost to breakage, where the filaments on the inside (close to center axis) were not. An explanation for how this could happen was shown in Chapter 3 equation 2, the filament strain was derived as a function of TPI and radius. When plotted in Figure 3.7, the strain gradient between the center axis and OD becomes highly non-linear as the twist increases past 3TPI. Using published filament breakage strain as a threshold, the maximum TPI that can be applied to the yarn without decreasing overall load lies somewhere between 3 and 5TPI.

6.3 Comprehensive Conclusions

The models created by AMSL's FiberPack code can accurately predict strength of ring spun and twisted yarn by capturing both tortuosity and pre-load. By using these models

with an explicit solver such as Sierra Solid Mechanics, yarn damage and dynamic failure can be accurately modeled.

The AMSL finite element analysis has shown that when 600 Denier Kevlar yarn is twisted past 3TPI, the pre-strain of the outside fibers cause localized failure that starts on the yarn O.D. and grows inward. The outside filaments are pre-strained due to the angular rotation varying by radius r_n. Ring spun yarn should not have the same dependence on twists per inch since the twist is added during structure creation instead of as a second step as in the case of the Kevlar yarn.

Since damage starts on the outer yarn filaments, there may be ways increase the yarn strength by twisting past 3TPI. One way to improve functionality would be to develop a variable twist as a function of yarn radius. In this manner the inside would be spun to a larger twist than the outside reducing the outside stress. Alternatively, the outside may be treated with a flexible urethane that slightly increases the failure strain. The FEA models built can aid in down selection for these methods of increasing overall yarn strength before complex tests are created.

Chapter 7 : Future Research

7.1 Improvements to test methodology

The old grip design consisted of a male and female V-notch coated with rubber. During tensile testing, the rubber became worn and came off; duct tape was used to line the grips and hold the filament. The grips were originally tightened with a four bolt pattern; this design was hard to apply an even pressure alloying yarn slip. New grips were created that pinched the yarn between two parallel flat plates lined with a more durable rubber superglued onto the metal. One plate is held fixed and the other is on two rods holding the plates parallel. A bolt was used to close and tighten the grip. It is has been showed that the force of the preload during twist is an important variable that can affect the load vs. strain response at TPI larger than 3. The current method of twisting the yarn by hand is time consuming and prone to error, due to the large amount of twists necessary. Additionally, it is hard to apply an exact preload onto the yarn during twist. One planned improvement for our tensile yarn test fixture is an automatic twisting apparatus. The new twisting apparatus will apply a specified load and auto-count the twists being applied to the specimen.

To ensure an accurate TPI count, a yarn twisting apparatus is being designed. The grips themselves will hold the fibers in place and then be turned either via hand crank or electric motor. An analog counter will keep track of the number of rotations the fiber will make, which can easily be translated to TPI via the following relation ($TPI=N/L$) where N is the number of rotations and L is the length of fiber between the grips. The rotation action side of the twister will only be allowed to rotate but the opposite end will be on a sliding mechanism in order to not overly pre-stress the fibers. After the fiber reaches the correct

number of twists, the grips are then removed from the apparatus and placed back in the fiber test mechanism.

7.2 Improving Analytical Model

The analytical model derived in chapter 3 is able to predict the correct trends in tenacity as a function of yarn twist ratio. The predicted failure load force for the 0 and 3TPI case was higher than the test showed. This was due to the stiffness of the analytical model was about1.28x higher than the stiffness reported by Gao [63] for the 0 and 3TPI cases. It was much closer for the 10 and 20TPI cases. For this research AMSL used a filament modulus reported by ARL that was 84.6 GPa [5], the filament modulus reported by Gao was 63 GPa [63]. The moduli are off by 1.34. More researchers have reported the larger modulus so that was used in the analytical equation. When AMSL used the lower moduli the analytical prediction was much closer to Gao's yarn tests.

This thesis proposes that there is a piece of physics missing from the analytical model. The finite element model's stiffness (based on a filament stiffness of 84.6GPa) matched Gao's and AMSL's tests data. The only piece of physics the finite element model had that was not built into the analytical equation set was filament tortuosity throughout the yarn length. Once the yarn is axially displaced and the filaments are consolidated on the yarn cross section, the FEA model showed that the filaments interwoven nature can create nodes where the filaments lock together locally.

The analytical equation also assumes a close packing of density 0.906 which is the solution for rigid disks. If the filament cross section is allowed to deform increasing the packing density to 1.0, and a solution is obtained for 0, 3, 10 and 20 TPI. The predicted

load responses match much closer to the test cases. The load response to elongation for each twist is plotted in Figure 7.1.

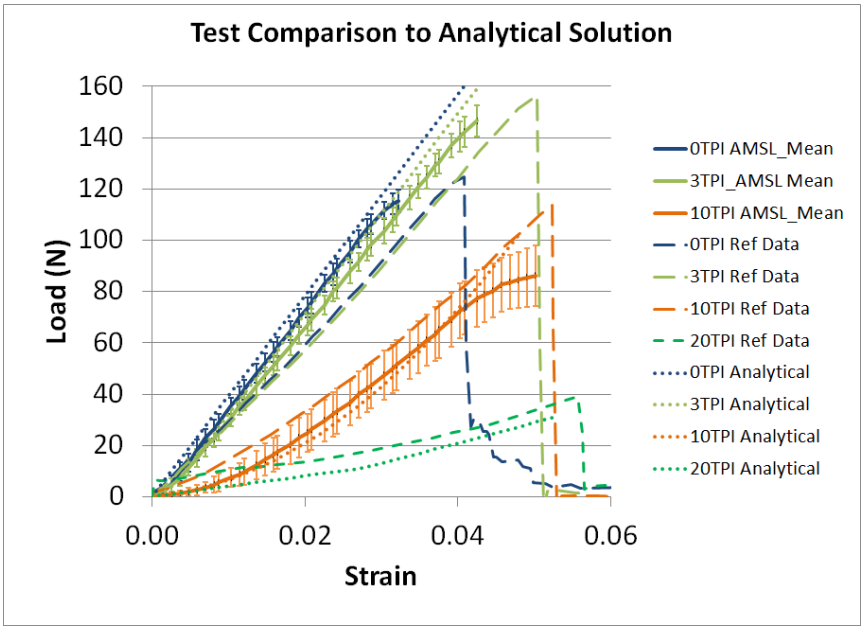

Figure 7.1 *By increasing the cross sectional packing density from theoretical maximum of 0.906 to 1.0 in the analytical solution, the analytical prediction can match the test data.*

One explanation for how the packing density can be closer to 1 would be transverse stiffness of the filaments if very low (1.34 GPa) as compared to it's axial modulus (84.6 GPa). Since the filament is soft in the transverse direction, the circular cross section can compress into a more optimal packing shape, thus allowing a packing density larger than the close packing density of circles (0.906).

The AMSL analytical model developed from physics seen in the AMSL finite element model and trends observed during tests, can accurately capture the non linear yarn stiffness change as the yarn is twisted from 0 to 20TPI. The noted failure strain prediction equation can accurately predict failure strain of the twisted yarn of twists up to 20TPI. To research the limitations of this model future work should be conducted measuring gauge

length change during twist at a constant axial pre-load. In addition, twisted yarn should be potted in acrylic freezing the cross sectional filament deformation to capture the cross sectional deformation and packing density as a function of twist. The FEA developed, along with the analytical model can be used to probe how to increase yarn tenacity for use in composite structures (tires), chords, and weaves.

Acknowledgements of Previous Publications

This thesis is composed in part of independent articles that have been published previously, are currently in press or are under review. Specifically, part of the material in Chapters 1 and 2 are results from (S. S. Recchia et al, "A Hierarchical Model for Kevlar Fiber Failure," *Proceedings of the ASME 2013 IMECE,* p. 4, 2013). Chapter 3 is composed of material published in (S. S. Recchia, J. Zheng and A. A. Pelegri, "Fiberwalk: a random walk approach to fiber representative volume element creation," *Acta Mechanica,* vol. 225, pp. 1301-1312, 2014.). Chapter 4 is being published in (A. A. Pelegri et al, "Multiscale modeling of randomly interwoven fibers for prediction of KM2 Kevlar yarn strength and damage," *Acta Mechanica (in publish),* 2015.)

Bibliography

[1] Y. Rao and R. J. Farris, "A Modeling and Experimental Study of the Influence of Twist on the Mechanical Properties of High-Performance Fiber Yarnds," *Journal of Applied Polymer Science,* vol. 77, no. (2000), pp. 1938-1949, 1999.

[2] M. Grujicic, W. C. Bell, P. S. Glomski, B. Pandurangan, C. F. Yen and B. A. Cheeseman, "Filament Level Modeling of Aramid Based High Performance Structural Materials," *Journal of Materials Engineering and Performance,* p. 1401:1413, 2011.

[3] G. Nilakantan, A. A. Obaid, M. Keefe and J. W. Gillespie, "Experimental evaluation and statistical characterization of the strength and strain energy density distribution of Kevlar KM2 yarns: exploring length-scale and weaving effects," *Journal of Composite Materials published online 8 November 2010,* vol. DOI: 10.1177/0021998310387667, p. 22, 2010.

[4] S. Recchia, J. K. Clawson, K. Sahin, K. Chasiotis, J. Zheng and A. A. Pelegri, "A Hierarchical Model for Kevlar Fiber Failure," *International Conference and Exposition of Mechanical Engineering, ASME, San Diego, CA, Nov 15-21, 2013 accepted for publication,* 2013.

[5] M. Cheng, W. Chen and T. Weerasooriya, "Mechanical Properties of Kevlar KM2 Single Fiber," *Journal of Engineering Materials and Technology,* vol. 127, no. APRIL, pp. 197-203, 2005.

[6] M. Grujicic, W. C. Bell, P. S. Glomski, B. Pandurangan, C. F. Yen and B. A. Cheeseman, "Filament Level Modeling of Aramid Based High Performance Structural Materials," *Journal of Materials Engineering and Performance,* vol. 20, p. 1401:1413, 2011.

[7] M. Dobb, D. J. Johnson, A. Majeed and P. S. B, "Microvoids in Aramid Type Fibrous Polymers," *Polymer,* vol. 20, October 1979.

[8] "ASTMD7269 Standard Test Methods for Tensile Testing of Aramid Yarns," ASTM International, West Conshohocken, PA, 2011.

[9] Sierra Solid Mechanics Team, "Presto 4.16 Users Guide," Sandia National Labs, Albaquerque, 2010.

[10] Sierra Solid Mechanics Team, "Theory Manual," Sandia National Lab, Albaquerque, NM, 2014.

[11] D. J. Benson, "Stable time step estimation for multi-material eulerian hydrocodes," *Computer Methods for Applied Mechanics of Engineering,* vol. 167, pp. 191 - 205, 1998.

[12] D. P. Flanagan and T. Belytschko, "Simultaneous relaxation in structural dynamics," *Journal of The Engineering Mechanics Division ASCE,* vol. 107, pp. 1039 - 1055, 1981.

[13] N. M. Newmark, "A method of computation for structural dynamics," *Journal of Engineering Mechanics, ASCE,* vol. 85, no. EM3, pp. 67 - 94, 1959.

[14] H. M. Hilber, T. J. R. Hughes and R. L. Taylor, "Improved numerical dissipation for time integration algorithms in structural dynamics.," *Earthquake Engineering and Structural Dynamics,* vol. 5, pp. 283 - 292, 1977.

[15] B. N. Parlett, "The symmetric eigenvalue problem Number 20," *Classic Applied Mathematics,* vol. SIAM, 1998.

[16] S. S. Recchia, J. Zheng and A. A. Pelegri, "Fiberwalk: a random walk approach to fiber representative volume element creation," *Acta Mechanica,* vol. 225, pp. 1301-1312, 2014.

[17] L. Iorga, Y. Pan and A. A. Pelegri, "Analysis of 3D random chopped fiber reinforced composites using FEM and random sequential adsorption," *Computational Materials Science,* vol. 43, no. 3, pp. 450-461, 2008.

[18] X.-Q. Feng, Q.-H. Qin and S.-W. Yu, "Quasi-micromechanical damage model for brittle solids with interacting microcracks," *Mechanics of Materials,* vol. 36, pp. 261-273, 2004.

[19] S. J. Hollister and N. Kikuchi, "A comparison of homogenization and standard mechanics analyses for periodic porous composites," *Computational Mechanics,* vol. 10, pp. 73-95, 1992.

[20] Y. J. Liu and X. L. Chen, "Evaluations of the effective material properties of carbon nanotube-based composites using a nanoscale representative volume element," *Mechanics of Materials,* vol. 35, pp. 69-81, 2003.

[21] S. Li, M. D. Thouless, A. M. Waas, J. A. Schroeder and P. D. Zavattieri, "Use of a cohesive-zone model to analyze the fracture of a fiber-reinforced polymer-matrix composite," *Composites Science and Technology,* vol. 65, no. 3-4, pp. 537-549, 2005.

[22] B. X. Shan, A. A. Pelegri and Y. Pan, "Interfacial Crack Kinking Subjected to Contact Effects," *Journal of Mechanics of Materials and Structures,* vol. 3, no. 4, pp. 591-605, 2008.

[23] S. S. Recchia, A. A. Pelegri and et. al, "A Hierarchical Model for Kevlar Fiber Failure," *Proceedings of the ASME 2013 International Mechanical Engineering Congress adn Exposition,* p. 4, 2013.

[24] V. Favier, R. Dendievel and G. Canova, "Simulation and modeling of three-dimensional percolating structures: Case of a letex matrix reinforced by a network of cellulose fibers," *Acta Materialia,* vol. 45, no. 4, pp. 1557-1565, 1997.

[25] S. K. Cousins and R. M. Brown, "Cellulose 1 microfibril assembly: computational molecular mechanics energy analysis favours bonding by van der Waals forces as teh initial step in crystallization," *Polymer,* vol. 36, no. 20, pp. 3885-3888, 1995.

[26] X. Jia and R. A. Williams, "A packing algorithm for particles of arbitrary shapes," *Powder Technology,* vol. 129, pp. 175-186, 2001.

[27] Y. Lee, C. Fang, Y.-R. Tsou, L.-S. Lu and C.-T. Yang, "A packing algorithm for three-dimensional convex particles," *Granular Matter,* vol. 11, pp. 307-315, 2009.

[28] G. T. Nolan and P. E. Kavanagh, "Random packing of nonspherical particles," *Powder Technology,* vol. 84, no. 3, pp. 199-205, 1995.

[29] W. A. Gray, The packing of solid particles, London: Chapman & Hall, 1968.

[30] W. Zhang, "Experimental and Computational Analysis of Random Cylinder Packins with Applications," *A dissertation submitted to Louisiana State University and Agricultural and Mechanical College,* 2006.

[31] G. Zhou and X. Sun, "Multi-chain digital element analysis in textile mechanics," *Composites Science and Technology,* vol. 64, pp. 239-244, 2003.

[32] T.-C. Lim, "three-level hierarchical approach in modeling sheet thermoforming," *International Journal of Mechanical Sciences,* vol. 45, pp. 1097-1117, 2003.

[33] B. Boubaker, B. Haussy and J.-F. Ganghoffer, "Consideration of the yarn-yarn," *Mechanics Research Comminucations,* vol. 34, pp. 371-378, 2007.

[34] E. D'Amato, "Finite element modeling of textile composites," *Composite Structures,* vol. 54, no. 2001, pp. 467-475.

[35] H. Altendorf and D. Jeulin, "Random Walk Based Stochastic Modeling of 3D Fiber Systems," *Physical Review,* vol. 83, p. 10, 2010.

[36] L. Berhan and A. M. Sastry, "Modeling percolation in high-aspect-ratio fiber systems. ii. the effect of waviness on the," *Physics Review,* vol. 75, p. 4:041121, 2007.

[37] N. Aboolfathi, A. Naik, M. Chafi, G. Karami and M. Ziejewski, "A micromechanical procedur for modelling the anisotropic mechanical properties of brain white matter.," *Computer Methods in Biomechanics and Biomedical Engineering,* vol. 12, pp. 249-262, 2009.

[38] D. I. Shreiber, H. L. Hao and R. Elias, "Probing the influence of myelin and glia on the tensile properties of the spinal cord.," *Biomechanics and Modeling in Mechanobiology,* vol. 8, pp. 311-321, 2009.

[39] Y. Pan, D. I. Schreiber and A. A. Pelegri, "A Transition Model for Finite Element Simulation on Kinematics of Central Nervous System White Matter," *IEEE Transactions on Biomedical Engineering, Special Issue: Multi-Scale Modeling and Analysis for Computational Biology and Medicine,* 2011.

[40] C. L. Johnson, M. McGarry, A. A. Gharibans, J. B. Weaver, K. D. Paulsen, H. Wang, W. C. Olivero, B. P. Sutton and J. G. Georgiadis, "Local Mechanical Properties of White Matter Structures in the Human Brain," *NeuroImage,* vol. 79, pp. 145-152, 2013.

[41] K. J. Streitberger, E. Wiener, J. Hoffmann, F. B. Freimann, D. Klatt, J. Braun, K. Lin, J. McLaughlin, C. Sprung, R. Klingebiel and I. Sack, "In Vivo Viscoelastic Properties of the Brain in Normal Pressure Hydrocephalus," *NMR in Biomedicine,* vol. 24, pp. 385-392, 2011.

[42] Y. Pan, V. Patel, A. A. Pelegri and D. I. Shreiber, "Psuedo 3D RVE Based Finite Element Simulation on White Matter," *Proceedings of the ASME 2012 International Mechnical Engineering Congress and Exposition,* 2012.

[43] B. J. Hamilton, "Process and Product Data Management for Staple Yarn Manufacturing," A thesis submitted to the Graduate Faculty, North Caorlina State University, 2010.

[44] A. Majumdar and S. Mukhopadhyay, "Properties of Ring Spun Yarns Made from Cotton and Regenerated Bamboo," *Indian Journal of Fibre and Textile Research,* vol. 36, pp. 18-23, March 2011.

[45] Z. Zupin and K. Dimitrovski, "Mechanical Properties of Fabrics Made from Cotton and Biodegradable Yarns Bamboo, SPF, PLA in Weft," *Woven Fabric Engineering,* 2010.

[46] A. A. Pelegri, S. S. Recchia, J. Q. Zheng and S. Horner, "Multiscale modeling of randomly interwoven fibers for prediction of KM2 Kevlar yarn strength and damage," *Acta Mechanica (in publish),* 2015.

[47] N. H. T. S. Administration, "The Pneumatic Tire," U.S Department of Transportation, DOT HS 810 561, Feb. 2006.

[48] X.-L. (. U. o. T. a. D. Gao, "A final report given to U.S Army PEO Office: Tensile Test Results of the Dyneema SK76 1500-dtex Yarn and Kevlar KM2 600-denier Yarn at different twist levels," Contract No.: W91CRB-07-D-0032-0005 (Mod 01), Period of Performance: 01/23/2011 – 08/31/2012.

[49] S. S. Recchia, A. A. Pelegri, J. Zheng, I. Chasiotis, J. K. Clawson and K. Sahin, "A Hierarchical Model for Kevlar Fiber Failure," *Proceedings of the ASME 2013 International Mechanical Engineering Congress adn Exposition,* p. 4, 2013.

[50] W. G. Knauss and I. Chasiotis, "Experimentation at the Micron-Submicron Scale," *Elsevier Science,* Vols. 8, Comprehensive Structural Integrity, no. Interfacial and Nanoscale Failure, pp. 41-87, 2003.

[51] M. Dobb, D. J. Johnson, A. Majeed and P. S. B, "Microvoids in Aramid Type Fibrous Polymers," *Polymer,* vol. 20, pp. 1284-1288, October 1979.

[52] M. Naraghi, I. Ozkan, M. P. de Boer, S. Hazra and S. S. Chasiotis, "MEMS platform for on-chip nanomechanical experiments with strong and highly ductile nanofibers," *Journal of Micromechanics and Microengineering,* vol. 20, pp. 125022-1-9, 2010.

[53] C. W. Verberne, "Mechanical Modelling of Textitles," University of Technology, Eindhoven, 2010.

[54] M. Loikkanen, G. Praveen and D. Powell, "Simulation of Ballistic Impact on Composit Panels," 2008.

[55] Sandia National Labs, "Cubit Home Manual," Albaquerque, NM, 2015.

[56] S. Corporation, "Abaqus 6.12 Analysis Users Manual, Volume V," Dassault Systemes, Providence, RI, 2010.

[57] H. Kong, C. Teng, X. Liu, J. Zhou, H. Zhong, Y. Zhang, K. Han and M. Yu, "Simultaneously Improving the tensile strength and modulus of aramid fiber by enhancing amorphous phase in supercritical carbon dioxide," *Royal Society of Chemistry Advances,* vol. 4, pp. 20599 - 20604, 2014.

[58] A. Dorigato and L. Fambri, "Effect of aramid regnerated fibers on thermo-mechanical behavior of polyamide 12 composites," *Reinforced Plastic & Composites,* vol. 32, no. 17, pp. 1243 - 1256, 2013.

[59] K. B. Cheng, T. W. Cheng, K. C. Lee, T. H. Ueng and W. H. Hsing, "Effects of yarn constitutions and fabric specifications on electrical properties of hybrid woven fabrics," *Composites: Part A,* vol. 34, pp. 971-978, 2003.

[60] B. Terry and K. Slater, "Comparitive analysis of synthetic fibres for marine ropes," *Journal of Consumer Studies & Home Economics,* vol. 22, pp. 19-24, 1998.

[61] D. Liu, C. Zhu, K. Peng, Y. Guo, P. R. Cheng and X. Cao, "Facile Preparation of Soy Protein/Poly(vinyl alcohol) Blend Fibers with High Mechanical Performance by Wet-Spinning," *Industrial & Engineering Chemistry Research,* vol. 52, pp. 6177-6181, 2013.

[62] National Highway Traffict Saftey Administration, "The Pneumatic Tire," U.S Department of Transportation, DOT HS 810 561, Feb. 2006.

[63] X.-L. Gao, "Tensile Test Results of the Dyneema SK76 1500-dtex Yarn and Kevlar KM2 600-denier Yarn at different twist levels," Department of Mechanical Engineering, The University of Texas at Dallas, Richardson, TX 75080, August, 2012.

[64] T. J. Mulkern and M. N. Raftenberg, "Kevlar KM2 Yarn and Fabric Strength Under Quasi-Static Tension," in *ARL-TR-2865,* Aberdeen, MD, 2002.

[65] H. W. Yang, H. J. Kim, C. Y. Zhu and Y. Huh, "Comparisons of Core-Sheath Stucturing Effects on the Tensile Properties of High-Tenacity Ring Core-Spun Yarns," *Textile Research Journal,* vol. 79, no. 5, pp. 453-460, 2009.

[66] M. Shioya, T. Itoh, T. Kunugi and A. Takaku, "Variation of longitudinal modulus with twist for yarns composed of high modulus fibers," *Textile Research Journal,* vol. 71, no. 10, pp. 928-937, 2001.

[67] A. A. Obaid, J. M. Deitzel, J. W. Gillespie and J. Q. Zheng, "The effects of environmental conditioning on tensile properties of high performance aramid fibers at near-ambient temperatures," *Journal of Composite Materials,* vol. 45, no. 11, pp. 1217 - 1231, 2011.

[68] B. Sanborn and T. Weerasooriya, "Quantifying damage at multiple loading rates to Kevlar KM2 fibers due to weaving, finishing, and pre-twist," *International Journal of Impact Engineering,* vol. 71, pp. 50-59, 2014.

[69] G. Zhou, X. Sun and Y. Wang, "Multi-chain digital element analysis in textile mechanics," *Composites Science and Technology,* vol. 64, pp. 239-244, 2003.

[70] B. Boubaker, B. Haussy and J.-F. Ganghoffer, "Consideration of the yarn–yarn interactions in meso/macro discrete model of fabric," *Mechanics Research Comminucations,* vol. 34, pp. 371-378, 2007.

[71] C. W. Verberne, "Mechanical Modelling of Textitles, A Literature Survey, Report number MT10.1," University of Technology, Eindhoven, May 2010.

[72] X. Liu and W. Yu, "Static Torsion and Torsion Fatigue of UHMW-PE and Aramid Filaments," *High Performance Polymers,* vol. 17, pp. 593-603, 2005.

[73] Y. Wang and Y. M. Xia, "Experimental and Theoretical Study on the Strain Rate and Temperature Dependence of Mechanical Behavior of Kevlar Fibre," *Compsites Part A: Applied Science and Manufacturing,* vol. 30, pp. 1251-1257, 1999.

[74] J. R. Koteras and R. B. Lehoucq, "Estimating the critical time-step in explicit dynamics using the Lanczos method.," *International Journal for Numerical Methods of Engineering,* vol. 69, no. 13, p. 2780, 2006.